Gustiness in thermally-stratified urban turbulent boundary-layer flows and the influence of surface roughness

G. Duan[a,*], T. Takemi[a]

[a]*Disaster Prevention Research Institute*
Kyoto University
Kyoto, Japan

Abstract

Gustiness is examined for the wind speed, fluctuations, turbulence intensities and fluxes for a real urban topography. Using large-eddy simulation (LES) **and an ensemble sampling approach, which allows a more comprehensive characterisation of the urban morphological features**, a wide range of boundary-layer stabilities is considered: the bulk Richardson number, $\mathrm{Rb} \in [-0.41,\ 0.82]$. Ratios of the proposed gustiness statistics, $\mathcal{G}$, over the conventional time-averaged flow and turbulence statistics are maximised for $z/H_{\mathrm{ave}} \lesssim 1$ (where H_{ave} is the mean building height). The strong linear scaling of $\mathcal{G}$ with the plan-area index (λ_p) for neutral stratification is found to persist for stably- and unstably-stratified flows ($R^2 \sim 0.8$). By contrast, the non-dimensionalised building-height variability, $\sigma_H/H_{\mathrm{ave}}$, and the effective frontal-area index, $\hat{\lambda_f} \equiv \lambda_f H_{\mathrm{ave}}/\sigma_H$, are argued to be of more appropriateness as scaling parameters for $\mathcal{G}$ compared to their original forms, σ_H and λ_f. **While the sensitivity of $\mathcal{G}$ to Rb is well defined at greater heights, the influence of surface inhomogeneity may be strong enough to oppose the effect of thermal stratification in the lower surface layers. Qualitative differences in the sensitivities to the boundary-layer stability are narrowly distinguishable amongst the zeroth-, first- and second-order gustiness statistics. The results are relevant to the understanding of urban wind hazards.**

Keywords: Wind gusts, urban design, street canyon, boundary-layer stability, ensemble sampling

*Corresponding author
Email address: `g.duan@storm.dpri.kyoto-u.ac.jp` (G. Duan)

1. Introduction

Urban turbulent boundary-layer (TBL) flows are strongly perturbed by the roughness elements mounted on the ground (Wooding et al., 1973; Oke, 2006). Understanding the complex interaction between the flow and the obstacles is important for urban planning and building design towards optimised building aerodynamics (Belcher, 2005; Bou-Zeid et al., 2009; Ashie and Kono, 2011) and improved urban microenvironments (Britter and Hanna, 2003; Yassin and Ohba, 2012; Wang et al., 2019). In particular, the extremes of micrometeorological events, including strong winds and turbulence (or wind gusts, hereafter $\mathcal{G}$), that can lead to **wind hazards**, are crucial to the urban-climate and building-environment safety (Nakayama et al., 2012; Takemi et al., 2019; Knoop et al., 2019; Takemi et al., 2020).

The geometry and arrangement of the roughness elements affect the flow and turbulence. Asymmetric street canyons (Hoydysh and Dabberdt, 1988; Addepalli and Pardyjak, 2013) result in flow and turbulence structures differing greatly from symmetric ones (Murena et al., 2011; Ngan and Lo, 2016). The flow pattern may also be altered by varying roof shapes (Wooding et al., 1973; Korycki et al., 2016; Allegrini, 2018) or differential organisations of the building obstacles (Hagishima et al., 2009), e.g. aligned (Inagaki and Kanda, 2008; Duan and Ngan, 2019) or staggered (Coceal et al., 2007b; Xie et al., 2008). Efforts have been made to characterise the urban surface inhomogeneity using a set of convenient parameters, which include the building-packing densities,

$$\lambda_p \equiv \frac{A_p}{A_T} \quad \text{and} \quad \lambda_f \equiv \frac{A_f}{A_T}, \tag{1}$$

(where A_p is the total plan area, A_f the total frontal area of the roughness elements and A_T the total lot area (Grimmond and Oke, 1999)), the mean and maximum building heights (H_{ave} and $H_{\max}$) and the building-height variability (σ_H) (Britter and Hanna, 2003; Nakayama et al., 2011; Yoshida et al., 2018; Yoshida and Takemi, 2018). For convenience, hereafter

$$\mathcal{S} \equiv \{\lambda_p,\ \lambda_f,\ H_{\mathrm{ave}},\ H_{\max},\ \sigma_H\}. \tag{2}$$

This has proven useful. For example, micrometeorological method in determining the surface aerodynamics parameters (the roughness length, $\hat{z}$, and the zero-plane displacement height, d), which define the well known surface-layer scaling (Perry et al., 1969;

M. R. Raupach, 1991),

$$U = \frac{u_*}{\kappa}\ln(\frac{z-d}{\hat{z}}), \tag{3}$$

where u_* is the friction velocity and κ the von Kármán constant (usually assumed to be 0.4), can be simplified with the morphometric method, whereby $\hat{z}$ and d are parameterised with the surface morphometric parameters, $\mathcal{S}$ (e.g. Macdonald et al., 1998; Grimmond and Oke, 1999; Kanda et al., 2013). However, relevant studies have originated with the purpose of incorporating urban canopy influences into mesoscale modelling as flux sources or sinks via parameterisation (Cheng and Castro, 2002) rather than quantifying the sensitivity of the turbulent flow within the canopy per se to $\mathcal{S}$.

Applying urban computational fluid dynamics (CFD) techniques, the influence of urban morphology on the turbulent flow can be explicitly resolved (Hanna et al., 2006). For example, the flow regime inside an urban canyon has shown a well-defined classification according to the building-height-to-canyon-width aspect ratio (AR) (Hunter et al., 1992) and the canyon vortex dynamics for different AR has been explored using large-eddy simulation and Green's function (Ngan and Lo, 2016). While studies of the 2-D cases shed lights on the nature of flow inside street canyons (e.g. Murena and Mele, 2014; Ngan and Lo, 2017), urban TBL flows are essentially 3-D in realistic urban scenarios–the mean flow only represents a partial picture–the perturbations that originated from the urban surface heterogeneity and the roughness anisotropy would almost always lead to a more complicated urban TBL environment, which may not be solely described by the mean streamline geometries. Organised low-frequency coherent structures and high-frequency turbulence may dominate compared to the mean flow (Thomas and Foken, 2007). **Also, conventional time averages have often been applied to turbulence statistics (e.g. Duan and Ngan, 2019; Marucci and Carpentieri, 2020), wherein the extremes (or gusts) are smoothed out.**

Attempts have been sought to apply the instantaneous maximum as a diagnostic for wind gusts. He and Song (1999) defined the peak gust, u_{gust}, as the wind speed, u, that exceeds the time average, $\overline{u}$, by three times of the turbulence intensity ($u_{\mathrm{r.m.s.}}$), i.e. $u_{\mathrm{gust}} \geq \overline{u} + 3u_{\mathrm{r.m.s.}}$. A similar criteria was applied in Hayashi (1992). The occurrence of wind gusts was shown to be more frequent for $1.2 \lesssim u_{\mathrm{gust}}/\overline{u} \lesssim 1.8$ (Nakayama et al., 2012). However, gusts may not be robustly distinguished from instantaneous signals without ensemble averages given the fact that the urban flow is highly intermittent and unsteady.

Wind gusts may be quantified in a probabilistic way, e.g. by means of the Weibull distribution (Murakami and Fujii, 1983). Conditional sampling (e.g. Wallace, 2016) has also proven useful in filtering extreme turbulence fluxes with a specified bandwidth, α, $|-u'w'| > \alpha|\overline{u'w'}|$ (e.g. Duan and Ngan, 2019). Gusty signals may be also identified in the spectral space, e.g. using wavelet analysis, which enables the localisation of extremes in time (Knoop et al., 2019). The gust index has often been defined as the ratio of the local maximum wind speed over the local temporal mean or the freestream wind speed (e.g. Ahmad et al., 2017; Takemi et al., 2020). While this perhaps simplifies the analysis, it is not necessarily implied that higher-order gustiness statistics, e.g. turbulence intensities and fluxes, **would be of negligible effects** (Inagaki and Kanda, 2008; Anderson et al., 2015).

Wind gusts have been studied for realistic urban areas under the perturbation of strong typhoons (Takemi et al., 2019, 2020). It was shown that the gust index scaled monotonicaly with λ_p at two vertical levels, $z/H_{\mathrm{ave}} = 0.5$ and 1.0. The wind gusts were found to be maximised in major streets and districts with sparse buildings, i.e. for low λ_p. Similar results had been obtained in Ahmad et al. (2017) and it has been noted that the relationship at a higher vertical level was less conclusive compared to the pedestrian level ($\sim 2\,\mathrm{m}$). While urban wind gusts have been explicitly linked to the plan-area index, influences of other morphometric parameters remain uncertain, e.g. σ_H, the building-height variability, which affects the surface inhomogeneity but is independent of λ_p by definition. The sensitivity of $\mathcal{G}$ to $\mathcal{S}$ remains inadequately resolved.

Most importantly, effects of the boundary-layer stability, which could be of significant impacts on the sensitivity of $\mathcal{G}$ to $\mathcal{S}$, have received little attention (if any). Both the mean flow and turbulence could be more complicated in thermal stratification: the flow regime undergoes a transition as the boundary-layer stability changes from unstable to stable stratifications and the wind fluctuations may need to attain a certain threshold before they can be unambiguously identified as gusts (Duan and Ngan, 2019). It is desirable to confirm if the previous findings for neutral flow carry over to thermally-stratified urban TBLs.

The current study attempts to resolve the above issues pertinent to urban gustiness with emphases on the following aspects. 1. In addition to λ_p, the influence of other morphometric parameters are considered, specifically the frontal-area index and the building-height variability. The surface heterogeneity of a realistic urban (Sec. 2.1) is characterised in a more comprehensive manner by traversing a sampling unit of various dimensions and displacement distances across the entire domain (Sec. 2.2), which allows ensemble averaging and hence more robust results. 2. The influence of thermal stratification is examined by considering a wide range of boundary-layer stabilities using large-eddy simulation (LES) (Sec. 2.3). The bulk Richardson number, $\mathrm{Rb} \in [-0.41,\ 0.82]$, satisfies values observed in realistic urban environments. 3. The previous studies are complemented by also exploring second-order gustiness statistics, which include gustiness turbulence intensities, momentum and thermal fluxes (see Sec. 2.4).

The remaining part of the paper is organised as follows. Sec. 3 analyses the vertical distribution of the gustiness statistics. Sec. 4 is focused on the 10 m-height $\mathcal{G}$, wherein influences of building-packing indices (λ_p and λ_f) (Sec. 4.1) and building-height variability (σ_H) (Sec. 4.2) are studied. The sensitivity of $\mathcal{G}$ to the boundary-layer stability is summarised in Sec. 5. Summary and discussion are given in Sec. 6.

2. Methodology

2.1. Building topography

Fig. 1 shows the topography of the studied area. The building topography herein is obtained from the digital surface model (DSM) data at the horizontal resolution of 2 m provided by Kokusai Kogyo Co., Ltd. As in Yoshida et al. (2018), the domain is surrounded by a buffer region that filled with cubic roughness elements. This is to alleviate influences due to the building-height discontinuity that may arise from the periodic lateral boundary conditions. The lateral dimensions (width and length) of the cuboids are fixed at 10 m, the height set to the domain averaged building height, $H_{\mathrm{ave,g}}$, and the packing density to $\lambda_p = 0.06$. The dimensions of the domain are $L_x = 1504 \times \Delta x = 3008$ m in the streamwise (x), $L_y = 480 \times \Delta y = 960$ m in the spanwise (y) and $L_z \approx 500$ m in the vertical (z) directions. The spatial resolution in the lateral is homogeneous, i.e. $\Delta x = \Delta y = 2$ m, which has proven sufficient for simulations of thermally-stratified urban boundary layers (Keck et al., 2014; Gronemeier et al., 2017). In the vertical, $\Delta z_{\min} = 2$ m for $0 < z \leq 80$ m ($\sim 4 - 8H_{\mathrm{ave,g}}$) and the grid spacing is stretched for $z > 80$ m with a stretching factor of 1.08 until $\Delta z_{\max} = 16$ m, which is maintained up to the upper boundary of the domain. The ratio of the coarsest and finest Δz is $\Delta z_{\max}/\Delta z_{\min} = 8$. The maximum grid cell

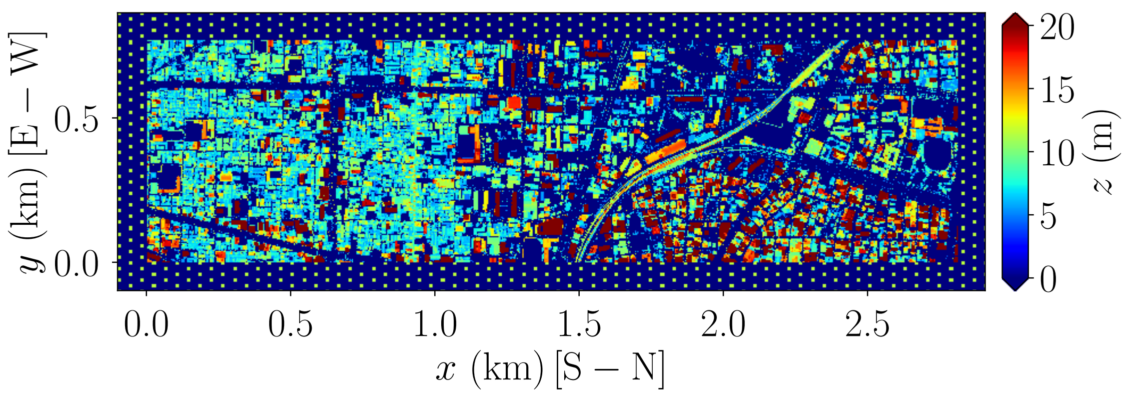

Figure 1: Topography of the studied domain, an urban area of Osaka, Japan. A buffer region filled with cubic blocks is set around the domain. The lateral dimensions of the cuboids are fixed at 10 m following Yoshida et al. (2018) and the height is equal to **the global average,** $H_{\mathrm{ave,g}} = 11.5\,\mathrm{m}$ **(the building height averaged for the entire domain). The maximum building heigh,** $H_{\mathrm{max,g}} = 58.2\,\mathrm{m}$**, and the standard deviation,** $\sigma_{H,\mathrm{g}} = 7.1\,\mathrm{m}$. The domain dimensions are summarised in Table 1. Fig. 3 plots the morphometric statistics.

Table 1: Domain dimensions and model parameters.

$L_x/\Delta x$	$L_y/\Delta y$	L_z (m)	$H_{\mathrm{ave,g}}$ (m)	$\sigma_{H,\mathrm{g}}$ (m)	$H_{\mathrm{max,g}}$ (m)
1504	480	500	11.5	7.1	58.2
$\Delta x = \Delta y$ (m)	Δz_{min} $(z \le 80)$ (m)	$\Delta z_{\mathrm{k+1}}/\Delta z_{\mathrm{k}}$ $(z > 80\,\mathrm{m})$		Δz_{max} (m)	
2	2	1.08		16	
ΔP_x $(\mathrm{Pa\,m^{-1}})$	$\xi \equiv t_f - t_0$ (s)	Δt (s)	Sampling unit, $\mathcal{D}$		
0.6×10^{-3}	3600	10	See Eqs. (4)-(7) and Fig. 2		

deformation is smaller than Cui et al. (2004) and Michioka et al. (2019) by a factor of ~ 2.

The domain dimensions and spatial resolutions are summarised in Table 1.

2.2. Sampling

The analysis areas are defined by traversing a sampling unit, $\mathcal{D}$, across the entire domain, i.e. $\mathcal{D} \in L_x \times L_y$. $\mathcal{D}$ is initially located at

$$\mathcal{D}_{0,0} \equiv A_0 \cap B_0, \tag{4}$$

where $A_0 \equiv [x_0, x_0 + l_x]$, $B_0 \equiv [y_0, y_0 + l_y]$ and $l_x \times l_y$ defines the total lot area covered by $\mathcal{D}$ (see Fig. 2 for a schematic illustration). $O(x_0, y_0) \equiv (0, 0)$ denotes the bottom-left corner of the domain (excluding the buffer region, see Fig. 1). The next analysis area is given by displacing $\mathcal{D}_{0,0}$ in the lateral directions, viz.

$$\mathcal{D}_{m,n} \equiv A_m \cap B_n, \tag{5}$$

where $A_m \equiv A_0 + m\Delta l_x$ and $B_n \equiv B_0 + n\Delta l_y$. The non-dimensional size of the sampling units,

$$l_x/\Delta x \in d_x, \tag{6a}$$

$$l_y/\Delta y \in d_y, \tag{6b}$$

are summarised in Table 2. The dimensions of $\mathcal{D}$ need to ensure that the profiles within each sampling unit are statistically representative. Cheng and Castro (2002) considered a spatial average over 25 sampling profiles and it was shown that a 4-profile average yielded very similar results. In the current study, the minimum quantity of profiles within each sampling unit is 125×125, which is larger compared to Cheng and Castro (2002) by two orders of magnitude. The non-dimensional displacement distances, Δl_x and Δl_y,

$$\Delta l_x/\Delta x \in s_x, \tag{7a}$$

$$\Delta l_y/\Delta y \in s_y, \tag{7b}$$

allow partial overlap of neighbouring $\mathcal{D}$ (see the green and blue patches in Fig. 2 for a schematic illustration). Through permutations and combinations of the sampling unit dimensions, Eq. (6), and the displacement distances, Eq. (7), the sample size is effectively increased, allowing a more comprehensive characterisation of the morphometric features of a realistic urban area (cf. Yoshida et al., 2018). For example, assuming $\Delta l_x = \frac{1}{2} l_x$ and $\Delta l_y = \frac{1}{2} l_y$, the sample size can be increased by a factor of up to $3 \sim 4$. Given the dimensions considered for the current domain (see Table 1), a dataset of about 4×10^3 analysis units is established.

For convenience, angle brackets denote horizontal averaging over each $\mathcal{D}$, viz.,

$$\langle \star \rangle = \frac{1}{A_{\mathcal{D}}} \int\limits_{A_{\mathcal{D}}} (\star) d\boldsymbol{x}, \tag{8}$$

where $A_{\mathcal{D}} = d_x \Delta x \times d_y \Delta y = l_x \times l_y$. For brevity, the notation will be dropped off for the gustiness statistics (see Sec. 2.4). For simplicity, the same notation is applied to ensemble

Table 2: Normalised dimensions and displacement distances of the sampling unit, $\mathcal{D}$ (Fig. 2).

d_x	d_y	s_x	s_y
$\{125, 150, 175\}$	$\{125, 150, 175\}$	$\{50, 100, 150\}$	$\{50, 100, 150\}$

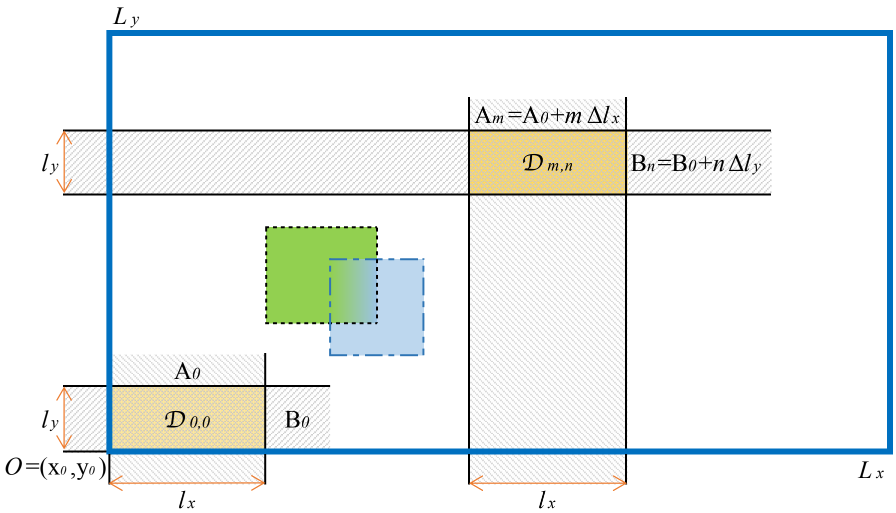

Figure 2: Schematic illustration of the sampling methodology. The sampling unit, $\mathcal{D}$, is initially located at $A_0 \cap B_0$ (i.e. $\mathcal{D}_{0,0} \equiv A_0 \cap B_0$), the bottom left corner of the domain, $L_x \times L_y$ (see Fig. 1 and Table 1), where $A_0 \equiv [x_0, x_0 + l_x]$ and $B_0 \equiv [y_0, y_0 + l_y]$. $\mathcal{D}_{m,n}$ denotes the updated sampling unit after displacing $\mathcal{D}_{0,0}$ in the streamwise direction by $m\Delta l_x$ and in the spanwise direction by $n\Delta l_y$. l_x and l_y are the lateral dimensions of $\mathcal{D}$, Eq. (6), and Δl_x and Δl_y are the displacement distances, Eq. (7). The green and blue patches denote that neighbouring $\mathcal{D}$'s are allowed to overlap.

averaging over the sampling units,

$$\langle \star \rangle \equiv \frac{1}{M \times N} \sum_{\mathcal{D}_{0,0}}^{\mathcal{D}_{M,N}} (\star), \tag{9}$$

where $M \times N$ denotes the maximum number of the urban unit, $\mathcal{D}$, that the domain can accommodate given the unit dimensions and displacement distances (see Fig. 2 and Table 2). Similar ensemble averaging was seen in Coceal et al. (2007a).

Applying the proposed sampling approach, a dataset of surface morphometric features is established. The morphometric metrics are graphed in a boxplot in Fig. 3, which includes the nominal minimum, maximum, the median and the 25%-75% quartiles. The values of each measure are roughly symmetrically distributed about the median, despite the plan-area index (λ_p) that is slightly positively skewed. λ_p also exhibits a greater variability compared to the frontal-area index (λ_f). The maximum building height ($H_{\max}$)

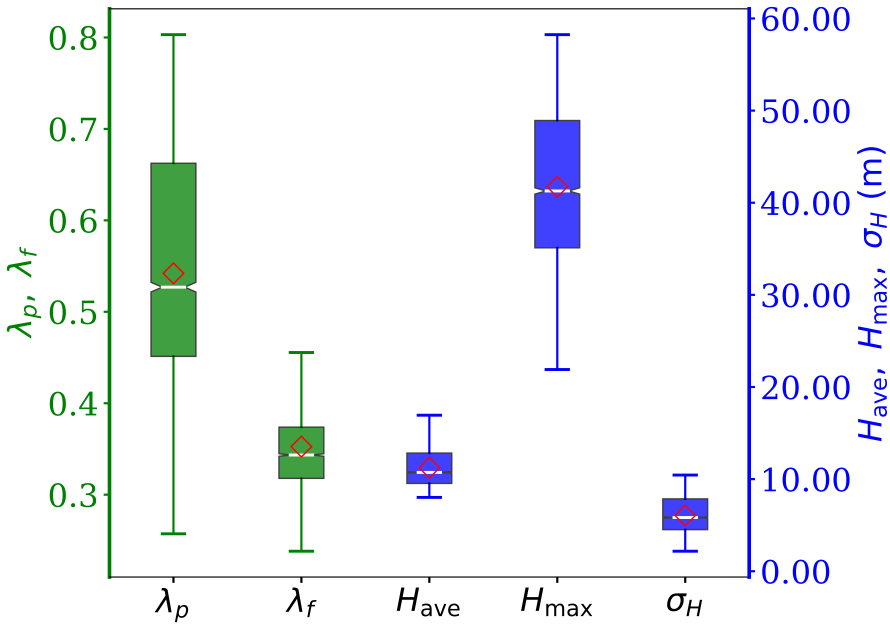

Figure 3: Morphometric statistics of the studied urban area (Fig. 1) applying the sampling approach proposed in Sec. 2.2. **The red diamond indicates the mean and the short horizontal line colored in white shows the median.**

shows a wide range of variation across the entire domain and is approximately four times of the mean building height (H_{ave}), indicating the presence of areas with a cluster of high-rise buildings. The morphometric statistics are similar to Kyoto (Takemi et al., 2020) and London, but differ greatly from some cities in North America~~n~~, e.g. Los Angeles (Ratti et al., 2002).

2.3. Large-eddy simulation

2.3.1. Numerical model

The flow and turbulence are simulated using large-eddy simulation based on the implicitly filtered non-hydrostatic, incompressible Boussinesq equations (Duan and Ngan, 2019; Wang and Anderson, 2019),

$$\frac{\mathrm{D}\tilde{\boldsymbol{u}}(\boldsymbol{x},t)}{\mathrm{D}t} == \frac{1}{\rho}\boldsymbol{F}(\boldsymbol{x},t) \tag{10}$$

where $\boldsymbol{F}$ denotes the forcing term, $\tilde{\boldsymbol{u}}$ is the velocity vector with its three components, $\tilde{u}$, $\tilde{v}$ and $\tilde{w}$, representing the projections on the streamwise (x), spanwise (or cross-stream, y) and vertical (z) axes of the coordinate vector, $\boldsymbol{x}$, respectively. The grid-filtered quantity, $\widetilde{(\cdot)}$, is obtained from convolution with a spatial filter kernel, $\tilde{\boldsymbol{u}} = G * \boldsymbol{u}(\boldsymbol{x},t)$. The resultant subgrid-scale (SGS) stress tensor, $\tau_{ij} = \widetilde{u_i u_j} - \widetilde{u}_i \widetilde{u}_j$, is parameterised using the modified 1.5-order Deardorff closure (Deardorff, 1980) of Moeng and Wyngaard (1988). The SGS eddy viscosity for momentum, $\nu_{\mathrm{sgs,m}}$, is modelled by solving a prognostic equation for the SGS turbulence kinetic energy. SGS parameterisation is also needed for the filtered energy equation (Bou-Zeid et al., 2010). The SGS eddy diffusivity for heat, $\nu_{\mathrm{sgs,h}}$, is modeled as $\nu_{\mathrm{sgs,h}} = \nu_{\mathrm{sgs,m}}/Pr_t$, where Pr_t is the turbulent Prandtl number and is slightly smaller than unity. For brevity, the tilde is dropped off hereafter. Coriolis accelerations are neglected.

The governing equations are solved using the LES model, PALM (Maronga et al., 2015). Third-order Runge-Kutta time-stepping scheme (Williamson, 1980) is combined with a fifth-order finite differencing scheme for momentum and scalar advection (Wicker and Skamarock, 2002). The Poisson equation for the pressure is solved with the multigrid method.

PALM has been extensively applied to studies of urban TBL flows (e.g. Letzel et al., 2008; Kanda et al., 2013; Park et al., 2015; Duan and Ngan, 2019). The model has been successfully validated for first-order statistics of temperature and velocity components (e.g. Yaghoobian et al., 2014; Park and Baik, 2013; Wang and Ng, 2018b). Second-order statistics also show good agreement with wind-tunnel measurements for thermally-stratified TBL flows (e.g. Duan and Ngan, 2020).

2.3.2. *Initialisation and forcing*

A thermally-stratified urban turbulent boundary-layer (TBL) flow is driven by a fixed pressure gradient in the streamwise direction, ΔP_x, which mimics an external large-scale forcing (e.g. Lo and Ngan, 2017), and a temperature difference specified between the ground surface, T_{ref}, and the freestream, T_0, $\Delta T \equiv T_{\mathrm{ref}} - T_0$ (see Table 3). The 3-D LES model is initialised from the stationary solution of a 1-D model based on the Reynolds-average turbulence parameterisation (Detering and Etling, 1985).

As in Cheng and Liu (2011), periodic boundary conditions are applied in the lateral directions and Neumann at the domain top. At solid surfaces, there is no-slip for the velocity components and Neumann for scalars, except for temperature on the ground, wherein Dirichlet boundary condition is used. A Prandtl layer is assumed between the roughness height, $z_0 = 0.1\,\mathrm{m}$, and the first grid level; the near-wall boundary conditions are parameterised following the Monin-Obukhov similarity theory (MOST). The occurrence of streak-like structures originating from the persistent periodic boundary conditions, also known as the spanwise locking of very large-scale structures (e.g. Hutchins and Marusic, 2007; Fang and Porté-Agel, 2015), is alleviated by applying 'shifted periodic boundary conditions' in the streamwise direction, whereby the outlet boundary no longer corresponds to the original inlet boundary but rather the one shifted in the spanwise direction (Munters et al., 2016). **The periodic boundary conditions herein differ from Duan and Ngan (2019), wherein turbulence recycling was combined with Dirichlet and radiation boundary conditions applied at the inlet and outlet boundaries, respectively, so as to mimic a neutrally-stratified flow approaching a local region that is thermally stratified. The current study requires horizontally-homogeneous statistics for both the velocity components and the temperature.**

The above model setups yield a thermally stratified TBL flow with the bulk Richardson number (e.g. Duan and Ngan, 2020),

$$\mathrm{Rb} = \left(\frac{g}{\overline{\overline{T}}} \frac{\tilde{\tilde{T}} - T_{\mathrm{ref}}}{\tilde{\tilde{H}}} \right) \Bigg/ \left(\frac{\tilde{\tilde{U}}}{\tilde{\tilde{H}}} \right)^2, \tag{11}$$

satisfying $\mathrm{Rb} \in [-0.41 \pm 0.08,\ 0.82 \pm 0.10]$, where $\tilde{\tilde{H}}$ denotes the canopy height (herein $\tilde{\tilde{H}} \sim H_{\max}$ as momentum fluxes peak close to the maximum building height (Kanda et al., 2013)), $\tilde{\tilde{T}}$ and $\tilde{\tilde{U}}$ the temporally- and spatially-averaged roof-level temperature and streamwise velocity, respectively, $\overline{\overline{T}}$ the temporally- and vertically-average temperature for $z/\tilde{\tilde{H}} \in [0, 1]$, $g = 9.8\,\mathrm{m\,s^{-2}}$ the gravitational acceleration. Similar boundary-layer stabilities have been considered in previous studies of urban TBL flows. For example, $\mathrm{Rb} \in [-0.52,\ 0.31]$ in the LES study of an idealised building array (Duan and Ngan, 2019), $\mathrm{Rb} \in [-0.21,\ 0.78]$ in wind-tunnel experiments (Uehara et al., 2000), $\mathrm{Rb} \in [-0.35,\ 0]$ from field measurements in a real city (Wang and Ng, 2018a) and $\mathrm{Rb} \in [-0.45,\ -0.17]$ from in situ measurements inside a street canyon (Nakamura and Oke, 1988).

The vertical scale may be limited by the domain height (L_z), which is smaller than the inversion height of a typical convective boundary layer. However, given the fact that only the flow and turbulence statistics in the surface layers are of great concern in the current study, it is a common practice to decrease the domain height to a reasonable level so that the simulations can

Table 3: **Temperature differences, $\Delta T \equiv T_{\text{ref}} - T_0$. T_{ref} denotes the temperature specified on the ground and $T_0 = 300\,\text{K}$ is the freestream temperature.**

Stability	–Stable–	–Neutral–	–Unstable–
ΔT (K)	{-8, -4}	{0}	{4, 8}

be accommodated without requiring an immerse amount of computer power (e.g. Kanda and Yamao, 2016; Nazarian and Kleissl, 2016; Duan and Ngan, 2019). In fact the current domain height is comparable with Park and Baik (2013), wherein turbulence coherent structures were studied for stably- and unstably-stratified urban TBL flows.

The Reynolds number based on $\tilde{\tilde{H}}$ and $\tilde{\tilde{U}}$, $Re = \tilde{\tilde{U}}\tilde{\tilde{H}}/\nu \sim \mathcal{O}(10^7)$, is consistent with the LES study of Wang and Anderson (2019) and the roughness Re, $Re^* = u_* \hat{z}/\nu \sim \mathcal{O}(10^6)$, comparable with the measured value of Inagaki and Kanda (2008) ($10^4 - 10^5$), where $\hat{z}$ denotes the roughness length that obtained via least-squares regression of the mean wind profiles in the logarithmic region (Cheng et al., 2007). The friction velocity, u_*, is calculated from the averaged Reynolds shear stress, $-u'w'$, at $z/\tilde{\tilde{H}} = 1$ (e.g. Kastner-Klein and Rotach, 2004), i.e. $u_* = (-\overline{u'w'})^{1/2}$. The stress may be averaged for the roughness sublayer (RSL) (e.g. $H_{\text{ave}} + \sigma_H < z < H_{\max}$, Kanda et al., 2013) or throughout the RSL and the inertial sublayer (ISL); however, this would not lead to a qualitatively differing result (Cheng and Castro, 2002).

For comparison, Rb, Re, Re^* and associated standard deviations are plotted in Fig. 4. The values of the Reynolds number and the bulk Richardson number for each ΔT are calculated from the ensemble average over the sampling units (see Eq. 9 in Sec. 2.2). The standard deviations therefore reflect the spatial variability.

The 3-D model is forced to develop for $t_f = 7$ hours, with a 6-hour spin up, $t_0 = 6\,\text{h}$. The last 1-hour data, $\xi \equiv t_f - t_0 = 3600\,\text{s}$, which are recorded every $\Delta t = 10\,\text{s}$ and have reached statistically-steady state, are used for analyses. For convenience, an overbar, $\overline{(\star)}$, will be used to denote the time averaging of the resolved-scale quantity, $(\star)$,

$$\overline{(\star)} \equiv \frac{1}{\xi} \int_{t_0}^{t_f} (\star)(t)\, dt, \tag{12}$$

and a single prime, $(\star)'$, the deviation from the time average, $(\star)' \equiv (\star) - \overline{(\star)}$.

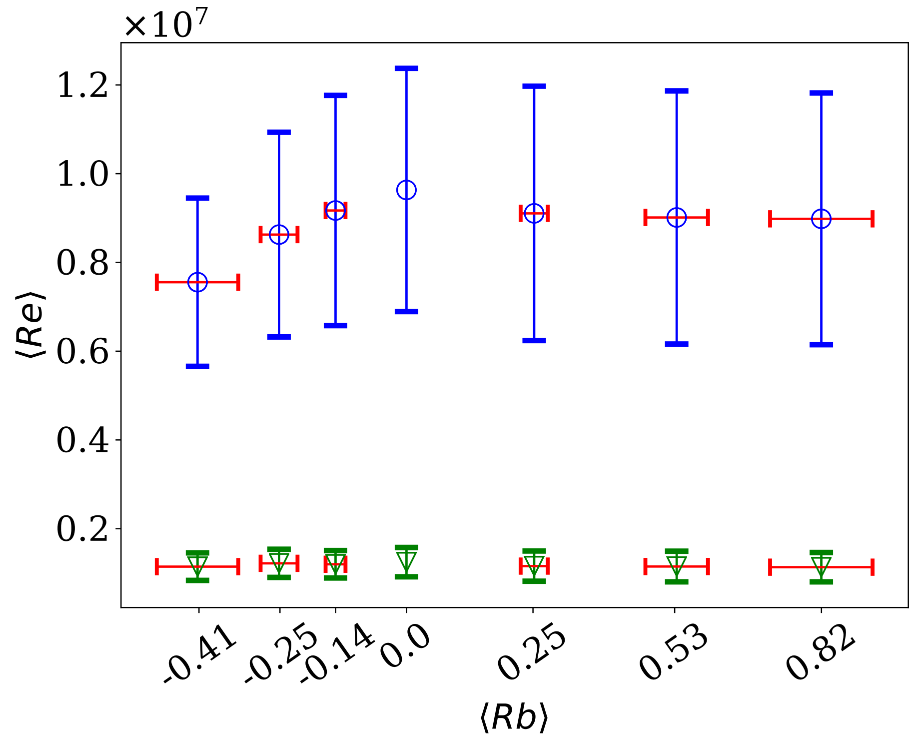

Figure 4: (Blue) Re; (green) Re^*; (red) Rb. The angle brackets denote the ensemble average over the sampling units (see Eq. 9 in Sec. 2.2). The error bars (standard deviations) reflect the spatial variability.

2.4. Gustiness and notation

Gustiness is defined as the extremes associated with either the resolved scale, e.g. u_i, or the turbulence quantity, e.g. u_i', viz.

$$|u_i|_{\max} \equiv \max_{\substack{t\in\xi \\ \vec{\mathbf{x}}\in\mathcal{D}}} |u_i(t,\vec{\mathbf{x}})|, \tag{13a}$$

$$|u_i'|_{\max} \equiv \max_{\substack{t\in\xi \\ \vec{\mathbf{x}}\in\mathcal{D}}} |u_i'(t,\vec{\mathbf{x}})|, \tag{13b}$$

$$\sigma_{u_i,\max} \equiv \max_{\substack{t\in \\ \vec{\mathbf{x}}\in\mathcal{D}}} u_i'^2(t,\vec{\mathbf{x}}), \tag{13c}$$

$$TKE_{\max} \equiv \max_{\substack{t\in\xi \\ \vec{\mathbf{x}}\in\mathcal{D}}} \frac{1}{2}(u'^2+v'^2+w'^2)(t,\vec{\mathbf{x}}), \tag{13d}$$

$$-|\varphi'\phi'_{(-)}|_{\max} \equiv -\max_{\substack{t\in\xi \\ \vec{\mathbf{x}}\in\mathcal{D}}} |\varphi'\phi'_{(-)}(t,\vec{\mathbf{x}})|, \tag{13e}$$

where $\xi \equiv t_f - t_0 = 3600\,\mathrm{s}$ (see Sec. 2.3.2), the subscript '$_{(-)}$' denotes negative fluxes[1], $u_i = \{u,v,w\}$, φ' and ϕ' ($\varphi' \neq \phi'$) denote the deviation of a velocity component (u_i)

[1]Negative covariances (known as sweeps or ejections in quadrant analysis) contribute to turbulence generation (Wallace, 2016).

or temperature (T) from the corresponding time average, Eq. (12). The extremes are calculated for all the grid points of each sampling unit, i.e. $\vec{\mathbf{x}} \in \mathcal{D}$ (see Sec. 2.2), and then horizontally averaged (see Eq. (8)). For convenience, a gust factor, $\mathcal{G}$, summarises all the gustiness statistics,

$$\mathcal{G} \equiv \{ \overbrace{|u_i|_{\max}}^{\text{Eq. (13a)}}, \underbrace{|u_i'|_{\max}}_{\text{Eq. (13b)}}, \overbrace{\sigma_{u_i,\max}}^{\text{Eq. (13c)}}, \underbrace{TKE_{\max}}_{\text{Eq. (13d)}}, \overbrace{-|\psi'\phi'_{(-)}|_{\max}}^{\text{Eq. (13e)}} \}. \tag{14}$$

The gustiness statistics may be non-dimensionalised with respect to the local temporal average (Nakayama et al., 2012), viz.

$$\mathcal{G} \equiv \begin{cases} |u_i|_{\max} / \langle \overline{u_i} \rangle, \\ |u_i'|_{\max} / \langle \overline{u_i'} \rangle, \\ \sigma_{u_i,\max} / \langle \overline{\sigma_{u_i}} \rangle, \\ TKE_{\max} / \langle \overline{TKE} \rangle, \\ -|\psi'\phi'_{(-)}|_{\max} / \langle \overline{\psi'\phi'} \rangle, \end{cases} \tag{15}$$

or the freestream reference quantities (e.g. Ahmad et al., 2017; Takemi et al., 2020), viz.

$$\mathcal{G} \equiv \begin{cases} |u_i|_{\max} / U_\infty, \\ |u_i'|_{\max} / U_\infty, \\ \sigma_{u_i,\max} / U_\infty, \\ TKE_{\max} / U_\infty^2, \\ -|\psi'\phi'_{(-)}|_{\max} / \psi_{\text{ref}}\phi_{\text{ref}}, \end{cases} \tag{16}$$

where U_∞ is the temporal and spatial average of the streamwise velocity in the horizontal plane close to the domain top and T_{ref} denotes the temperature specified on the urban floor (see Sec. 2.3.2), $\psi_{\text{ref}}\phi_{\text{ref}} = U_\infty T_{\text{ref}}$ for thermal fluxes and $\psi_{\text{ref}}\phi_{\text{ref}} = U_\infty^2$ for momentum fluxes. The former, Eq. (15), quantifies the gusts with respect to the local statistically-steady state, while the latter, Eq. (16), assesses the local extremes versus the large-scale forcing.

In urban microenvironments, the flow and turbulence are strongly perturbed by the roughness elements that mounted on the urban surface. Well-defined local steady states are generally difficult to be established within the roughness sublayer in realistic scenarios

(Ahmad et al., 2017). The dynamics of the flow are complicated by perturbations of ground heating or cooling (Duan and Ngan, 2019). By contrast, fully developed turbulent boundary layers are often seen above the roughness sublayer: TBLs have been shown for $z/H \gtrsim 1.5$ for idealised urban canyons (Park and Baik, 2013; Duan and Ngan, 2018) and $z/H_{\mathrm{ave}} \gtrsim 2-5$ for realistic ones (Rotach, 1995; Giometto et al., 2016). While gustiness is essentially local, the normalisation with respect to the freestream reference quantities may be more appropriate for the evaluation of influences of severe meteorological perturbations (e.g. strong typhoons, Takemi et al., 2019, 2020).

3. Vertical profiles

Vertical profiles are helpful in characterising the change of turbulence and gustiness statistics from inside the canyons to the boundary layers aloft the surface roughness and up to the top of the domain. Fig. 5 plots the vertical profiles of the gustiness statistics, $\mathcal{G}$, for different ΔT. Each profile corresponds to the horizontal average over a single (urban) sampling unit, $\mathcal{D}$ (see Sec. 2.2). **For clarity in the lower surface layers, a base-10 logarithmic scale is used for y axis and results of only one unit displacement, $s_x = s_y = 100$, but all unit sizes, $d_x \times d_y$ (see Table 2 in Sec. 2.2), are shown. Despite that the profiles are plotted for the gustiness, the general pattern resembles the conventional time-averaged flow and turbulence statistics that observed in wind-tunnel experiments for thermally-stratified TBL flows (Uehara et al., 2000).**

The sensitivity of $\mathcal{G}$ to λ_p depends on the vertical level. The **color gradients** are well defined for $z \lesssim H_{\max}$, implying a monotonic dependence of $\mathcal{G}$ on λ_p in the lower surface layers. This is consistent with previous studies for neutral flows, e.g. Ahmad et al. (2017), which was focused on the 2 m-height wind gusts, and Takemi et al. (2020), wherein the gusty winds were compared for $z/H_{\mathrm{ave,g}} = 0.5$ and 1.0. We note that the relationship between $\mathcal{G}$ and λ_p is inconclusive at higher vertical levels, $z \gtrsim H_{\max}$, **which coincides with Ahmad et al. (2017) that the surface aerodynamic roughness length was found to be of more relevance to $\mathcal{G}$ compared to the plan-area index at higher elevations above the canopy layer (though the study was conducted for only neutral stratification).** However, the influence of the surface obstacles does not vanish–the profiles associated with each ΔT do not exactly collapse.

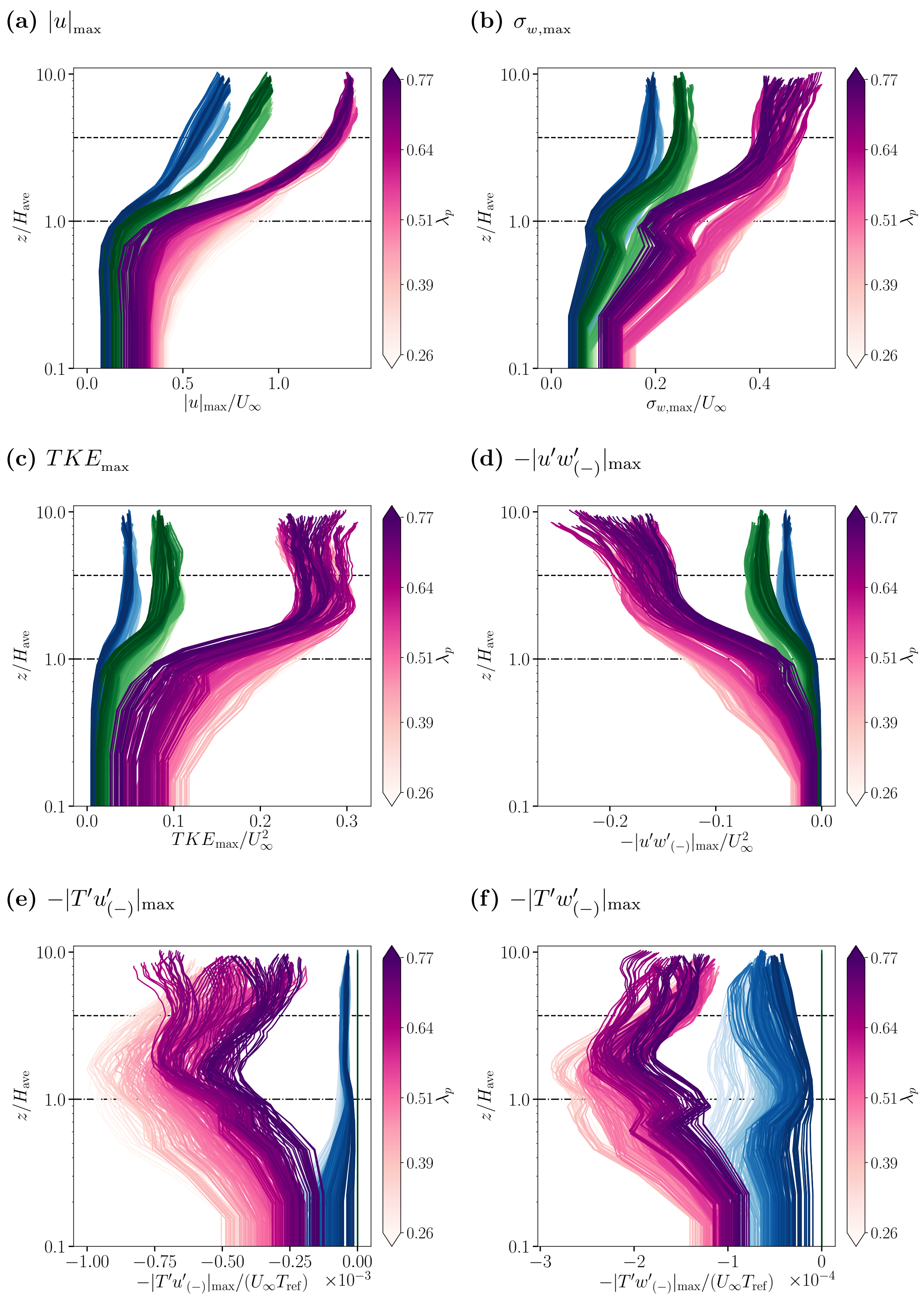

Figure 5: Vertical profiles of the normalised gustiness statistics, Eq. (16), for different ΔT. **(Blues) $\Delta T = -8\,^\circ$C; (greens) $\Delta T = 0\,^\circ$C; (purples) $\Delta T = 8\,^\circ$C. The profiles are colored in light (for low λ_p) and deep (for high λ_p) colors that associated with each ΔT. For brevity, the colorbar is only shown for $\Delta T = -8\,^\circ$C. The horizontal lines indicate the global values: upper dashed line for $H_{\rm max,g}$ and lower dash-dotted line for $H_{\rm ave,g}$ (see Table 1). Note the base-10 logarithmic scale for y axis.**

Unlike the conventional time-averaged turbulence statistics (Kastner-Klein and Rotach, 2004; Cheng et al., 2007; Roth et al., 2015), the profiles of the gustiness statistics do not converge at greater heights.

As in Raupach et al. (1996), $\mathcal{G}$ attain local maxima for $H_{\mathrm{ave}} \lesssim z < H_{\mathrm{max}}$ and there is a rapid decay with decreasing height for $z/H_{\mathrm{ave}} \lesssim 1$. Note $H_{\mathrm{ave,g}} \sim 10\,\mathrm{m}$ (see Table 1). Comparable 10 m−height $\mathcal{G}$ were found in urban areas of Osaka (Takemi et al., 2019) and Kyoto (Takemi et al., 2020) during the passage of a strong typhoon. The pedestrian-level $\mathcal{G}$ are also in good agreement with the LES study of wind gusts in Tokyo (Ahmad et al., 2017), $\mathcal{G} \sim \mathcal{O}(0.1)$.

The profiles also exhibit a strong dependence on the boundary-layer stability. While the sensitivity to ΔT seems monotonic for $z/H_{\mathrm{max}} \lesssim 1$, there is a slight overlap of neighboring profile bunches, indicating that the influence of surface inhomogeneity may be strong enough to oppose the effect of thermal stratification in certain regions of the domain–the 3-D details of urban roughness elements may be of non-negligible importance. By contrast, the influence of ΔT predominates away from the surface roughness–the three bunches of the profiles that associated with different ΔT are well separate at higher vertical levels.

The $\mathcal{G}$ statistics (except the thermal fluxes, panels e,f) are not maximised for $z/H_{\mathrm{ave}} \sim 1$ or $z/H_{\mathrm{max}} \sim 1$. This is because the normalisation is against the freestream reference parameters, U_∞ and T_{ref} (see Eq. (16)), rather than the local quantities (see Eq. (15)) and the turbulence production increasingly dominates for large fluctuations at greater heights.

Fig. 6 plots the point-wise comparison of the $\mathcal{G}$ intensities against the conventional time-averaged turbulence statistics. While the colormaps also indicate a rough monotonic dependence of the gustiness statistics on the building-height variability, this is less evident for the unstable case. **The ratios offer a general idea about the relative strength of gustiness over the time averages.** There is a well-defined convergence towards lower values as the height is increased **for $z/H_{\mathrm{ave}} \gtrsim 1$ and the maximum ratios are found to occur substantially inside the canyons ($z/H_{\mathrm{ave}} < 1$, note $H_{\mathrm{ave,g}} \sim 10\,\mathrm{m}$, see Table 1).** The dependence of the 10 m-height $\mathcal{G}$ on the urban morphometric parameters, $\mathcal{S}$, is investigated in greater detail in Sec. 4.

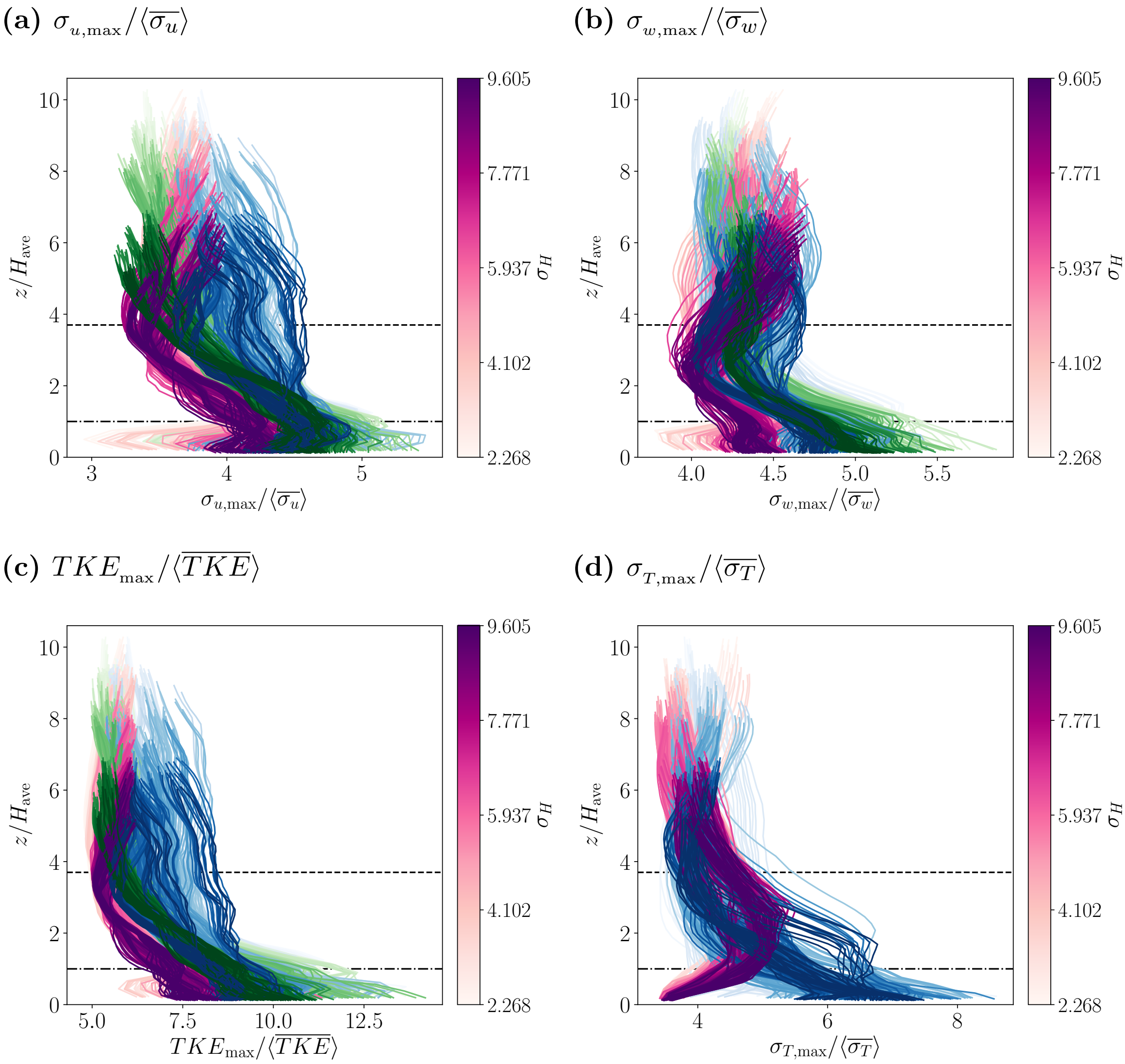

Figure 6: As in Fig. 5, but for the ratios of the gustiness intensities over the conventional time-averaged turbulence statistics, Eq. (15). **The profiles are colored by the building-height variability, σ_H (m), in the color associated with each ΔT. The colormaps follow that in Fig. 5. Angle brackets denote horizontal averaging over $\mathcal{D}$ (see Eq. (8)) and overline denotes the temporal average.**

4. 10 m-height gustiness statistics

Inside the urban canyons, the flow is strongly perturbed by the obstacles and the dynamics are more complex as the flow being thermally stratified. The most obvious evidence is the Reynolds shear stress, $-u'w'$, which is weakened in stably-stratified flows, whilst strengthened in unstable stratification. A direct influence is on the friction velocity, $u_* \propto \sqrt{|-u'w'|}$. Fig. 7 plots the normalised u_* against the non-dimensionalized σ_H **(panel a) and the building-packing indices (panel b)** for stable, neutral and unstable stratification. The friction velocity is reduced by $\sim 50\%$ in stable stratification ($\Delta T = -8\,°\mathrm{C}$) compared to the unstable case ($\Delta T = 8\,°\mathrm{C}$). A comparable reduction has been measured in wind-tunnel experiments of thermally-stratified flows in a 2-D canyon (Marucci and Carpentieri, 2019).

The increasing trend of u_*/U_∞ with $\sigma_H/H_{\mathrm{ave}}$ (panel a) admits the fact that the drag force is larger for urban surfaces of higher inhomogeneity (Cheng and Castro, 2002; Britter and Hanna, 2003), and this is especially so when the boundary layer is unstably stratified. By contrast, the colormap indicates a complicated influence of the normalised maximum building height, $H_{\max}/H_{\mathrm{ave}}$, on the drag. The surface inhomogeneity is not solely determined by the geometric parameters (e.g. σ_H and $H_{\max}$), but also affected by the building packing indices (panel b). Medium values of u_*/U_∞ are found to be clustered around the maximum λ_f (indicated in the colormap); however, this is not necessarily true for λ_p. Unlike the frontal-area index (λ_f), λ_p is not explicitly correlated with σ_H by definition (Grimmond and Oke, 1999). It plausible that the dependence of u_*/U_∞ on λ_p is also nonlinear. A likely explanation is that as λ_p approaches the theoretical limit, $\lambda_p \to 1$, the drag force returns to that for a flat plane (assuming $\sigma_H = 0$)–an intermediate range of λ_p may exist for the drag force to attain maximum values (Shaw and Pereira, 1982; Raupach, 1992). The idea also agrees with the rationale categorising the urban flow regimes (Hussain and Lee, 1980). The friction velocity reflects the combined effects of those different components that affect the surface homogeneity; however, disentangling the contribution of separate factors to the drag force is not straightforward.

Following the discussion in Sec. 3 and Takemi et al. (2019), this section analyses the

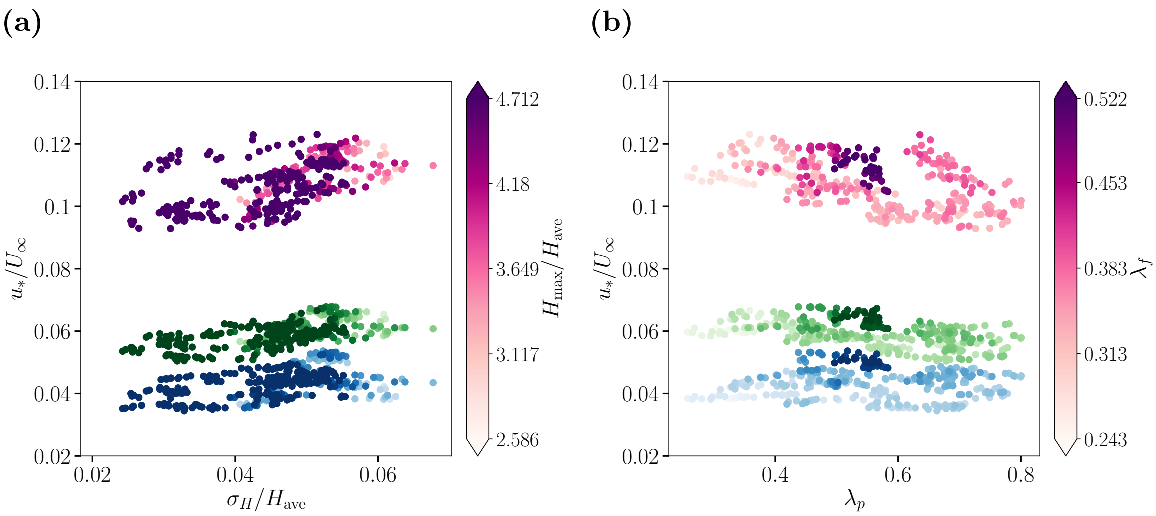

Figure 7: **Normalised friction velocity, u_*/U_∞, versus the (a) non-dimensional building-height variability and the (b) building-packing indices. (blues) $\Delta T = -8\,°\mathrm{C}$; (greens) $\Delta T = 0\,°\mathrm{C}$; (purples) $\Delta T = 8\,°\mathrm{C}$. The colormaps follow that in Fig. 5.**

10 m-height gustiness statistics. As the vertical level is increased, the plan-area index is decreased **and eventually the flow is devoid of direct perturbations from the surface roughness elements (Giometto et al., 2016).**

Fig. 8 plots the gustiness statistics in the $x - y$ plane at the 10 m height. There is a strong sensitivity to the boundary-layer stability: the extremes weaken in stable stratification (left panels), whilst strengthen in unstable stratification (right panels), which coincide with the pattern of the thermal flux (panels g,h). The sensitivity exhibits a great similarity to that for the conventional time-averaged turbulence statistics (e.g. Duan and Ngan, 2019).

The extremes are markedly visible in areas **of more sparsely distributed building obstacles (i.e. regions of low plan-area index as annotated in the white squares in panel b)**, which agrees well with previous studies (e.g. Ahmad et al., 2017; Takemi et al., 2020). The current study also shows that the pattern is well preserved irrespective of ground heating or cooling. The sensitivity of $\mathcal{G}$ to the surface morphometric parameters (λ_p, λ_f and σ_H) and the boundary-layer stability is investigated in the remaining sections.

4.1. Influence of building-packing indices, λ_p and λ_f

Fig. 9 plots the normalised $\mathcal{G}$ against λ_p. For $\Delta T = 0$ (the blues), $\mathcal{G}$ show a strong linear dependence on λ_p (e.g. $R^2 = 0.80$ for the gustiness TKE), wherein $\mathcal{G}$ are maximised for small λ_p and minimised for large λ_p. The results are consistent with the study of

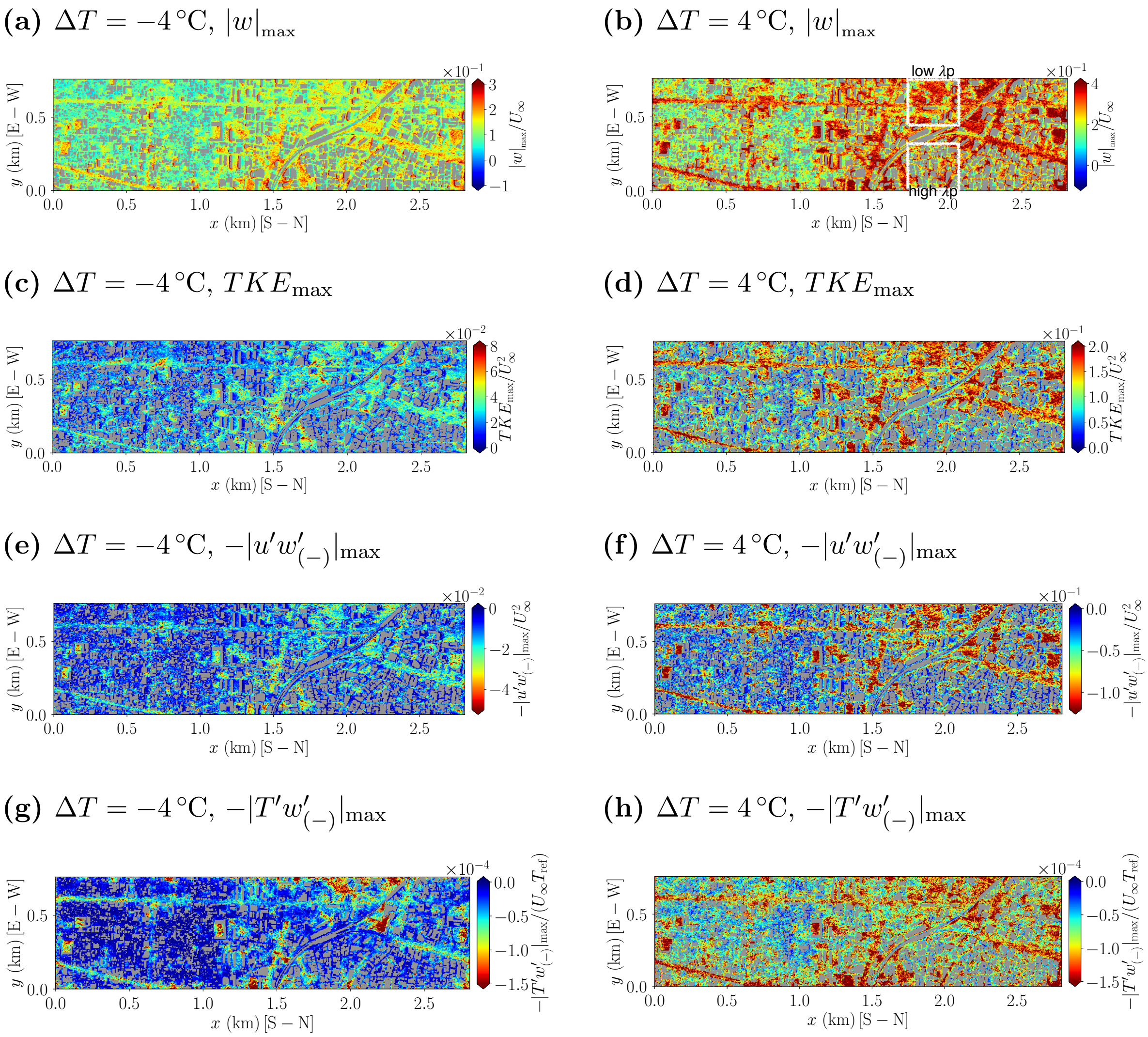

Figure 8: Normalised gustiness statistics, $\mathcal{G}$ (Eq. (14)), in the 10 m-height $x-y$ plane. (left panels) Stable stratification, $\Delta T = -4\,°\mathrm{C}$; (right panels) unstable stratification, $\Delta T = 4\,°\mathrm{C}$. (a-b) Vertical velocity component, $|w|_{\max}$; (c-d) turbulence kinetic energy, $TKE_{\max}$; (e-f) turbulent momentum flux, $-|u'w'_{(-)}|_{\max}$; (g-h) thermal flux, $-|T'w'_{(-)}|_{\max}$. **As the $\mathcal{G}$ statistics are approximately an order of magnitude smaller for the stable cases compared to the unstable ones (cf. Fig. 5), for visualisation purpose, the colorbars are capped at smaller values for stable stratification.**

Ahmad et al. (2017) for a neutrally-stratified TBL flow that developed over an urban area of Tokyo. **It is further confirmed herein that** the linear scaling of $\mathcal{G}$ with λ_p persists for stable and unstable stratifications. **By contrast, the colormap implies a strong non-linear relationship between $\mathcal{G}$ and the frontal-area index, λ_f (explored in the later text accompanying Fig. 10).**

The gustiness is considerably more sensitive to the change of ΔT, $d\Delta T$, for $\Delta T > 0$ compared to that for $\Delta T < 0$, i.e. $d\mathcal{G}/d\Delta T|_{\Delta T>0} > d\mathcal{G}/d\Delta T|_{\Delta T<0}$. For example, the trends of $\mathcal{G}$ versus λ_p for $\Delta T = -4\,°\mathrm{C}$ and $-8\,°\mathrm{C}$ almost collapse, while that for $\Delta T > 0$ are well separate. The slope is much steeper for the latter. More specifically, $\mathcal{G} \propto -0.03\lambda_p$ for $\Delta T = -8\,°\mathrm{C}$ and $\mathcal{G} \propto -0.18\lambda_p$ for $\Delta T = 8\,°\mathrm{C}$. Analogous results have been noted in Duan and Ngan (2019, 2020) for thermally-stratified flows developed over an idealised building array. While those studies were focused on the standard time-averaged turbulence statistics, the influence of ΔT on wind gusts was indicated in the quadrant analysis: stable flow is characterised with small fluctuations and the quadrant statistics change marginally with ΔT; however, sweeps diminish greatly for $\Delta T > 0$ as ΔT is increased and ejections dominate.

Fig. 10 plots the normalised $\mathcal{G}$ against the frontal-area index, λ_f. **Despite that the general pattern of $\mathcal{G}$ versus λ_p (Fig. 9) is roughly preserved (noticeably for high H_{ave} as indicated in the colormap), the dependence of gustiness on λ_f is non-linear:** the weakest gustiness appears to prioritise moderate λ_f that accompanied with low H_{ave} (highlighted in the ellipse between the vertical dash-dotted lines, see panel a) and this is especially so for $\Delta T > 0$. Also, we note that the quality of the linear curve fitting using least-squares regression is not good for both the stable and unstable cases, e.g. $R^2 = 0.22$ for $\Delta T = -8\,°\mathrm{C}$ and 0.35 for $\Delta T = 8\,°\mathrm{C}$ for the gustiness TKE, TKE_{max}.

By definition, λ_f should be small when the building height is low (Grimmond and Oke, 1999); however, this is not necessarily true for inhomogeneous surfaces. The results indicate that there exists regions of high σ_H to offset the decrease of λ_f due to the low averaged building height, H_{ave}. This may explain the concurrence of low H_{ave} with medium λ_f but not small λ_f, suggesting that an effective λ_f may be defined for inhomogeneous surfaces by incorporating σ_H and H_{ave} into the scaling. Following the idea in Kanda et al. (2013) ~~that~~ on a somewhat unrelated topic, it is sensible to combine the nondimensional quantity, $H_{\mathrm{ave}}/\sigma_H$, directly with λ_f, i.e.,

$$\hat{\lambda}_f \equiv \lambda_f H_{\mathrm{ave}}/\sigma_H. \tag{17}$$

An appreciable increase is seen in the R-squared with the effective λ_f, $\hat{\lambda}_f$, in place of the unscaled λ_f for the linear least-squares fitting (see Fig. 11), e.g. the R^2 for TKE_{max} is increased from 0.22 to 0.53 for $\Delta T = -8\,°\mathrm{C}$ and from 0.35 to 0.50 for $\Delta T = -8\,°\mathrm{C}$, suggesting that $\hat{\lambda}_f$ **is of a more appropriate scaling parameter for $\mathcal{G}$ compared to λ_f.**

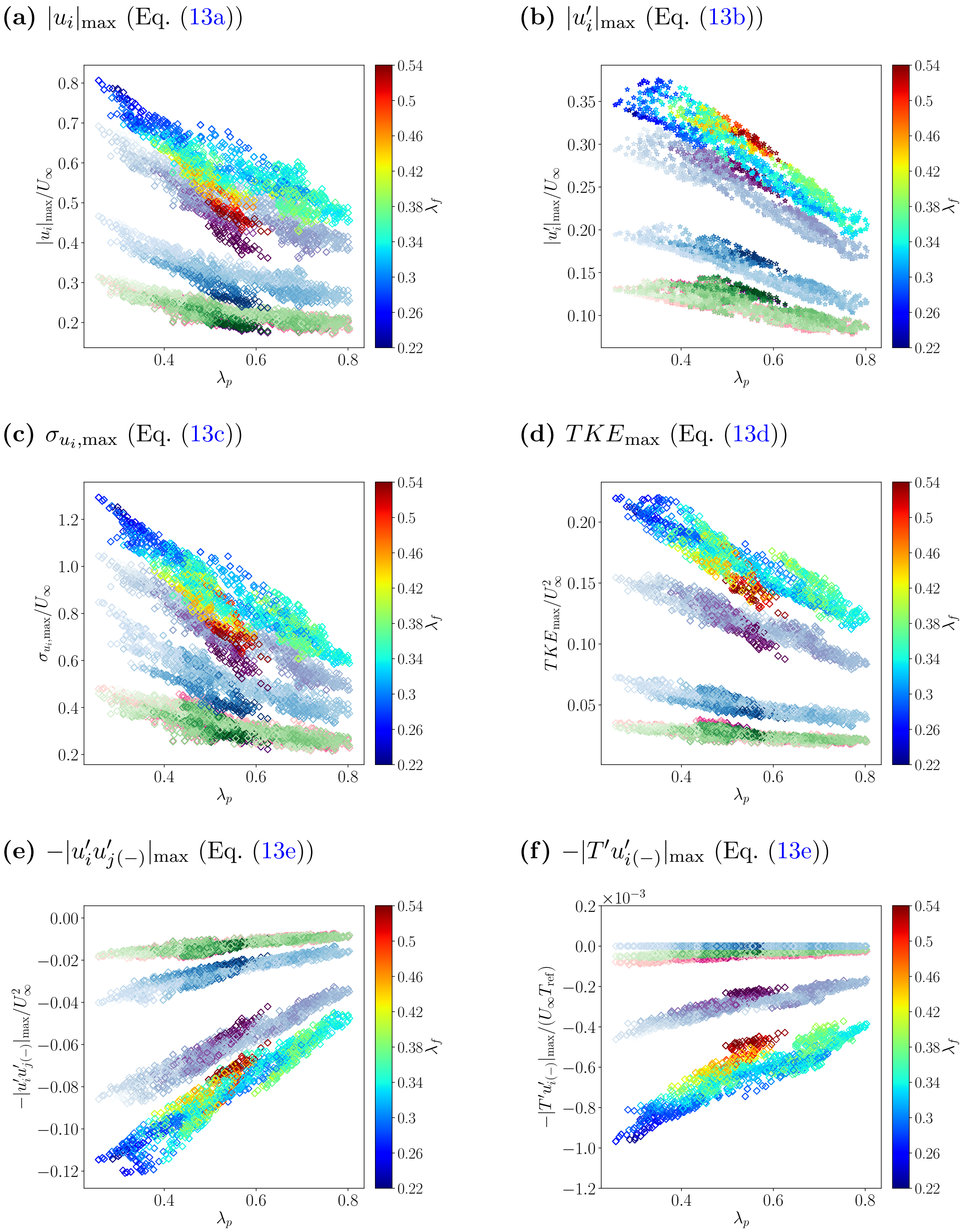

Figure 9: Normalised $\mathcal{G}$ versus λ_p. For brevity, results of only the streamwise velocity component are shown ($u_i = u$ and $u_i'u_j' = u'w'$); other components show similar trends. The gustiness statistics are colored by the frontal area density, λ_f: (gradient red) $\Delta T = -8\,^\circ$C; (gradient green) $\Delta T = -4\,^\circ$C; (gradient blue) $\Delta T = 0\,^\circ$C; (gradient purple) $\Delta T = 4\,^\circ$C; (red-green-blue) $\Delta T = 8\,^\circ$C. The trends for the stable cases nearly overlap. **For brevity, the colorbar is only shown for $\Delta T = 8\,^\circ$C. The colormaps for the other ΔT follow the convention that light colors indicate small values (herein λ_f) and deep for large ones.**

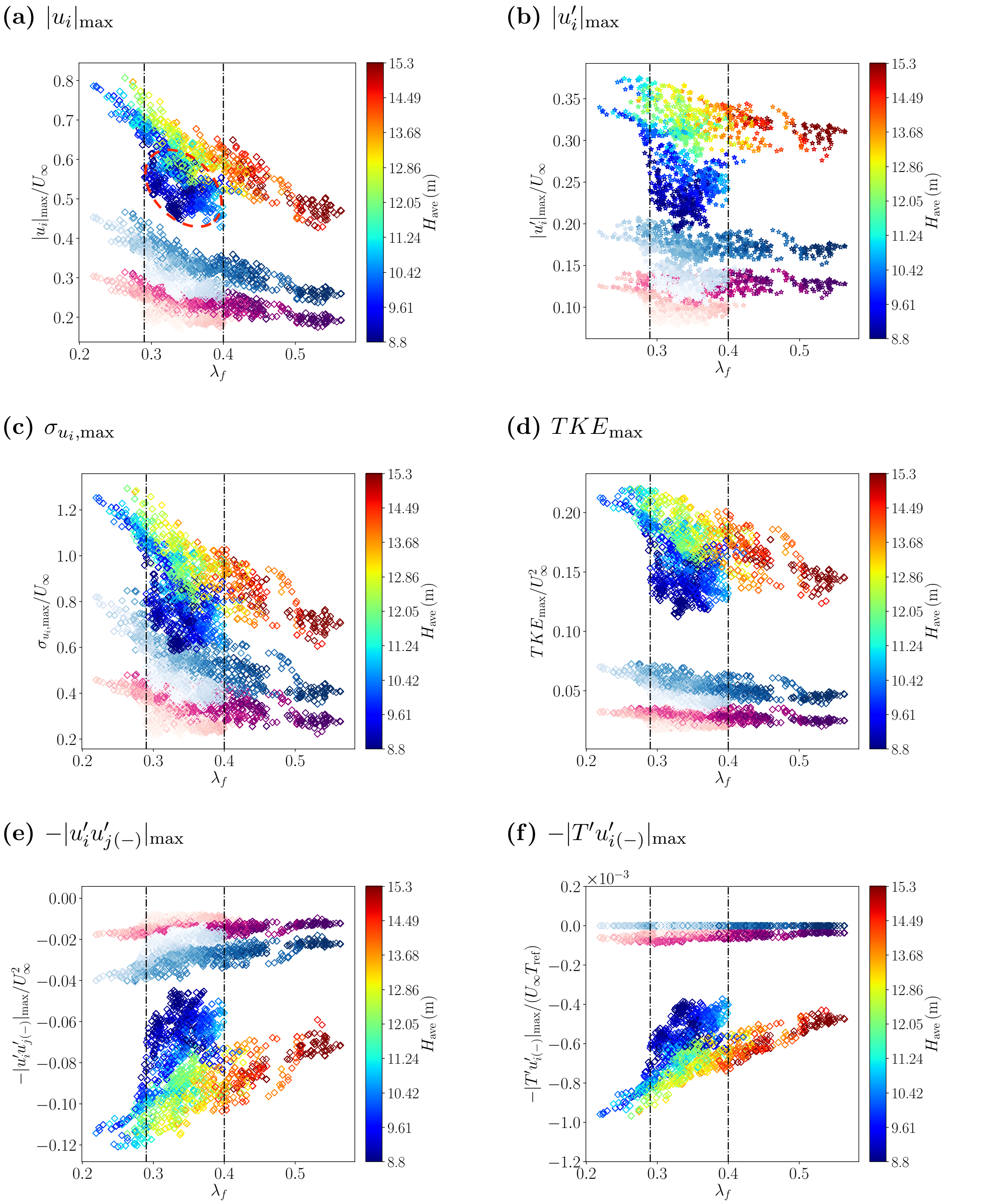

Figure 10: As in Fig. 9, but for λ_f, and colored by H_{ave}. For clarity, results of only one stable (gradient purple, $\Delta T = -8\,^\circ\mathrm{C}$), one neutral (gradient blue, $\Delta T = 0\,^\circ\mathrm{C}$) and an unstable (red-green-blue, $\Delta T = 8\,^\circ\mathrm{C}$) case are shown. **The colormaps follow that in Fig. 9.** The dashed ellipse in panel a highlights the minimal H_{ave} that obtained for moderate λ_f, $0.3 \lesssim \lambda_f \lesssim 0.4$, the range bounded between the dash-dotted vertical lines.

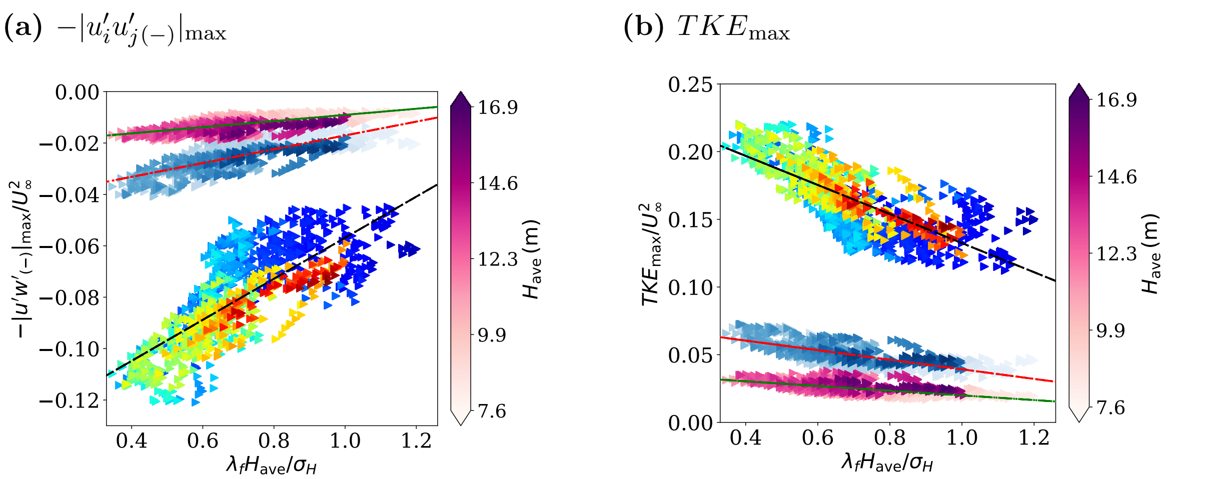

Figure 11: As in Fig. 10, but for $\mathcal{G}$ versus the effective λ_f, $\hat{\lambda_f}$ (i.e. $\lambda_f H_{\text{ave}}/\sigma_H$, see Eq. (17)). For brevity, only the gustiness momentum flux and the TKE are plotted. (a) $-|u_i'u_{j(-)}'|_{\max}$; (b) $TKE_{\max}$. Note the shift of low H_{ave} to high $\lambda_f H_{\text{ave}}/\sigma_H$ compared to the clustering of low H_{ave} around moderate λ_f in Fig. 10. The dash-dotted lines indicate the linear curve fitting using least-squares regression: $R^2 = 0.57$ for the gustiness flux (panel a) and $R^2 = 0.53$ for the gustiness TKE (panel b).

4.2. Influence of building-height variability, σ_H

A similar trend as that for $\mathcal{G}$ versus λ_p and λ_f (Sec. 4.1) may not be expected for $\mathcal{G}$ versus σ_H. This is because the building-height variability affects the frontal-area density but is independent of the plan-area density by definition.[2]

Fig. 12 plot the gustiness statistics versus the building-height variability, σ_H. For comparison, the dependence of $\mathcal{G}$ **on the building-packing indices are indicated in the colormaps: the left panels are colored by λ_p and the right by λ_f, but they plot the same data. Therefore, the plots agree with** Fig. 9 and Fig. 10, respectively.

The strongest $\mathcal{G}$ prioritise a certain range of σ_H, $4\,\text{m} \lesssim \sigma_H \lesssim 10\,\text{m}$ (or $0.35 \lesssim \sigma_H/H_{\text{ave}} \lesssim 0.9$), wherein both λ_p and λ_f attain smallish values (indicated in the colormaps). The smallest σ_H appears to be in concurrence with the largest λ_p on minimised $\mathcal{G}$, implying that the gustiness is weak in urban areas of high plan-area packing density and low building-height variability.

The dependence of $\mathcal{G}$ on σ_H differs for stable stratification compared to unstable

[2]This may be a contributing factor to the clustering of scattered $\mathcal{G}$ at low building heights for a certain range of λ_f (distinctly for unstable stratification, see Fig. 10), in contrast to the well defined linear scaling of $\mathcal{G}$ versus λ_p (see Fig. 9).

stratification. A familiar monotonic dependence (approximately linear) seems well preserved for $\Delta T \leq 0$. In stably-stratified flows, the (internal) boundary-layer thickness is suppressed (roughly to the roof level) (Duan and Ngan, 2020) and hence wind gusts are affected by the surface roughness obstacles in a more direct manner. However, the quality of the linear curve fitting using least-squares regression is actually not as good as the plots show (e.g. $R^2 = 0.37$ for TKE_{max}). For unstable stratification, $\mathcal{G}$ are more scattered ($R^2 = 0.26$) and the dependence on σ_H is even less definite for the second-order $\mathcal{G}$ statistics (see panels c-d, e-f). This may be attributed to the alignment of the vorticity, which is altered by the convective plumes. In a neutrally-stratified shear flow, the vorticity orientation is set by the symmetric, $\mathbf{S} = \frac{1}{2}\left(\nabla\tilde{\mathbf{u}} - \nabla\tilde{\mathbf{u}}^{\mathrm{T}}\right)$, and the anti-symmetric, $\mathbf{\Omega} = \frac{1}{2}\left(\nabla\tilde{\mathbf{u}} + \nabla\tilde{\mathbf{u}}^{\mathrm{T}}\right)$, components of the velocity gradient tensor, $\nabla\tilde{\mathbf{u}}$ (Wu et al., 2006). The vorticity is stretched by the former and rotated by the latter. The orientation towards the streamwise direction is a result of the balance between the strain-rate tensor and the rotation-rate tensor (Dubief and Delcayre, 2000). As the ground being heated or cooled, buoyancy competes against the shear. A direct measure to quantify the balance is the Richardson number, $Ri = N^2/S^2$, where N^2 is the buoyancy term and S^2 the shear term (also see Sec. 2.3.2). With the increase of the boundary-layer instability, buoyancy-induced vertical motions set in, tilting the alignment of the vorticity towards the vertical (Li and Bou-Zeid, 2011; Simpson and Glezer, 2016). As a consequence, vertical fluxes intensify up to greater heights (e.g. Kanda and Yamao, 2016) (roughly indicated in the peak ratios in Fig. 6, Sec. 3) and the influence of σ_H is effectively alleviated. Similar justification may be applied to the weakening influence of λ_p and λ_f on $\mathcal{G}$ at higher vertical levels that away from the surface perturbations.

The results suggest that σ_H may not be an appropriate scaling parameter for the gustiness statistics; however, we note that the quality of the linear curve fitting is improved when its normalised form (cf. Ratti et al., 2002), σ_H/H_{ave}, is used (see Fig. 13). For example, the R^2 of the least-squares regression for the gustiness momentum flux, $-|u_i'u_{j(-)}'|_{\text{max}}$ (panel a), is increased from 0.45 to 0.5 for $\Delta T = -8\,^{\circ}\mathrm{C}$ and from 0.36 to 0.45 for $\Delta T = 8\,^{\circ}\mathrm{C}$. **A comparable improvement is also seen for the gustiness TKE, TKE_{max} (panel b), e.g. from 0.37 to 0.43 for $\Delta T = -8\,^{\circ}\mathrm{C}$ and from 0.26 to 0.38 for $\Delta T = 8\,^{\circ}\mathrm{C}$. While the increase of the R-squared seems unremark-**

able, implying that σ_H may be of secondary importance for the scaling, the influence of building-height variability on the gustiness is non-negligible.

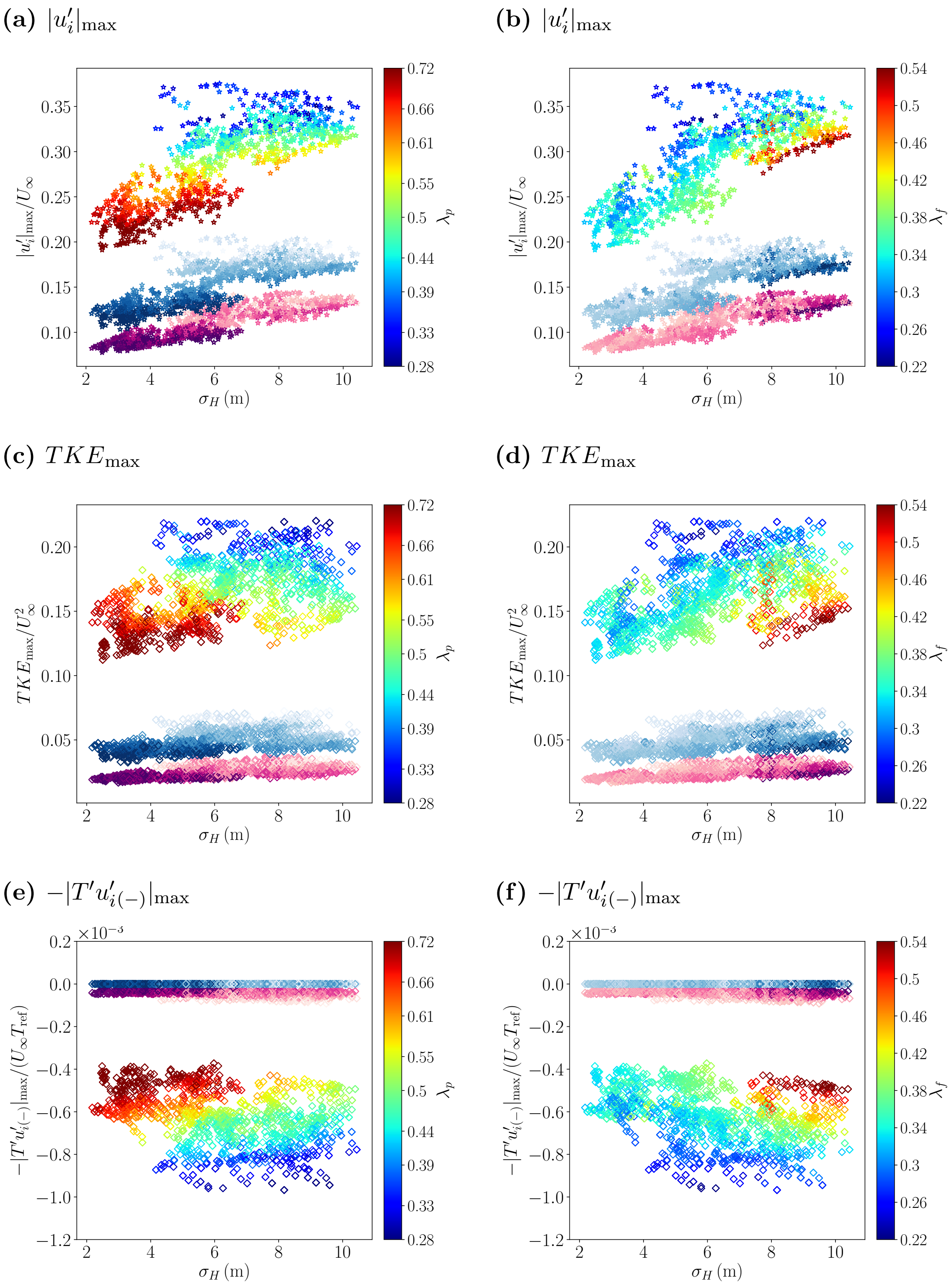

Figure 12: Normalised $\mathcal{G}$ versus σ_H. For comparison, (left panels) colored by λ_p as in Fig. 9; (right panels) colored by λ_f as in Fig. 10.

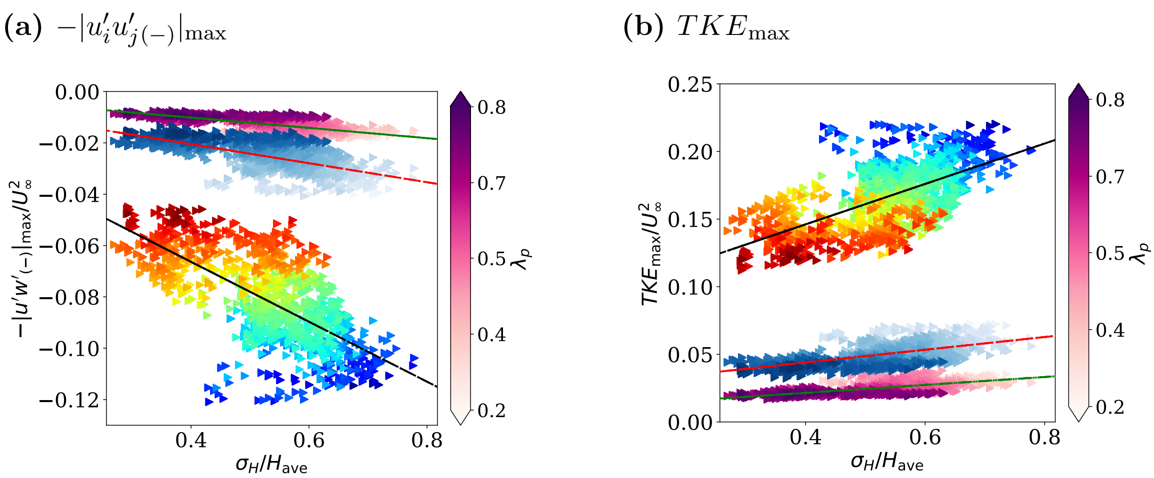

Figure 13: As in Fig. 11, but for $\mathcal{G}$ versus the normalised σ_H, σ_H/H_{ave}.

5. Sensitivity to Rb

Fig. 14 compares the **spatial and ensemble averages of the normalised gustiness TKE, $TKE_{\max}$, versus the boundary-layer stability and the plan-area index for $z/H_{\text{ave,g}} \in [0, 1]$ (panel a) and $z/200\,\text{m} \in [0, 1]$ (panel b)**. The gustiness TKE increases monotonically with the increasing of the boundary-layer instability (Rb ≤ 0) and plateaus for stable stratification (Rb > 0). Quadrant analyses have shown that large turbulence fluctuations are more sensitive to the boundary-layer stability (as that for Rb < 0), whilst small ones may need to exceed a certain threshold to become fully turbulent (as that for Rb > 0) (Duan and Ngan, 2019). The trends reconcile with previous studies for thermally-stratified TBL flows over idealised urban topographies (Uehara et al., 2000; Cheng and Liu, 2011; Duan and Ngan, 2019) (though for the conventional time-averaged turbulence statistics), implying that the sensitivity of time-averaged statistics of urban TBL flows to Rb is well preserved in the associated extremes.

The colormaps associated with each Rb reproduce the monotonic dependence of $TKE_{\max}$ on λ_p (almost linear, see Sec. 4.1). While $TKE_{\max}$ strengthens with decreasing λ_p, the influence of surface roughness weakens at greater heights–the color bins in panel b are greatly shortened compared to that plotted in panel a. Nevertheless, the general trend of $TKE_{\max}$ versus Rb is well maintained to higher vertical levels. The other gustiness quantities exhibit a similar sensitivity to Rb (summarised in Fig. 15). Qualitative differences in the sensitivities to the boundary-layer stability are narrowly distinguishable amongst the zeroth-, first- and second-order gustiness statistics.

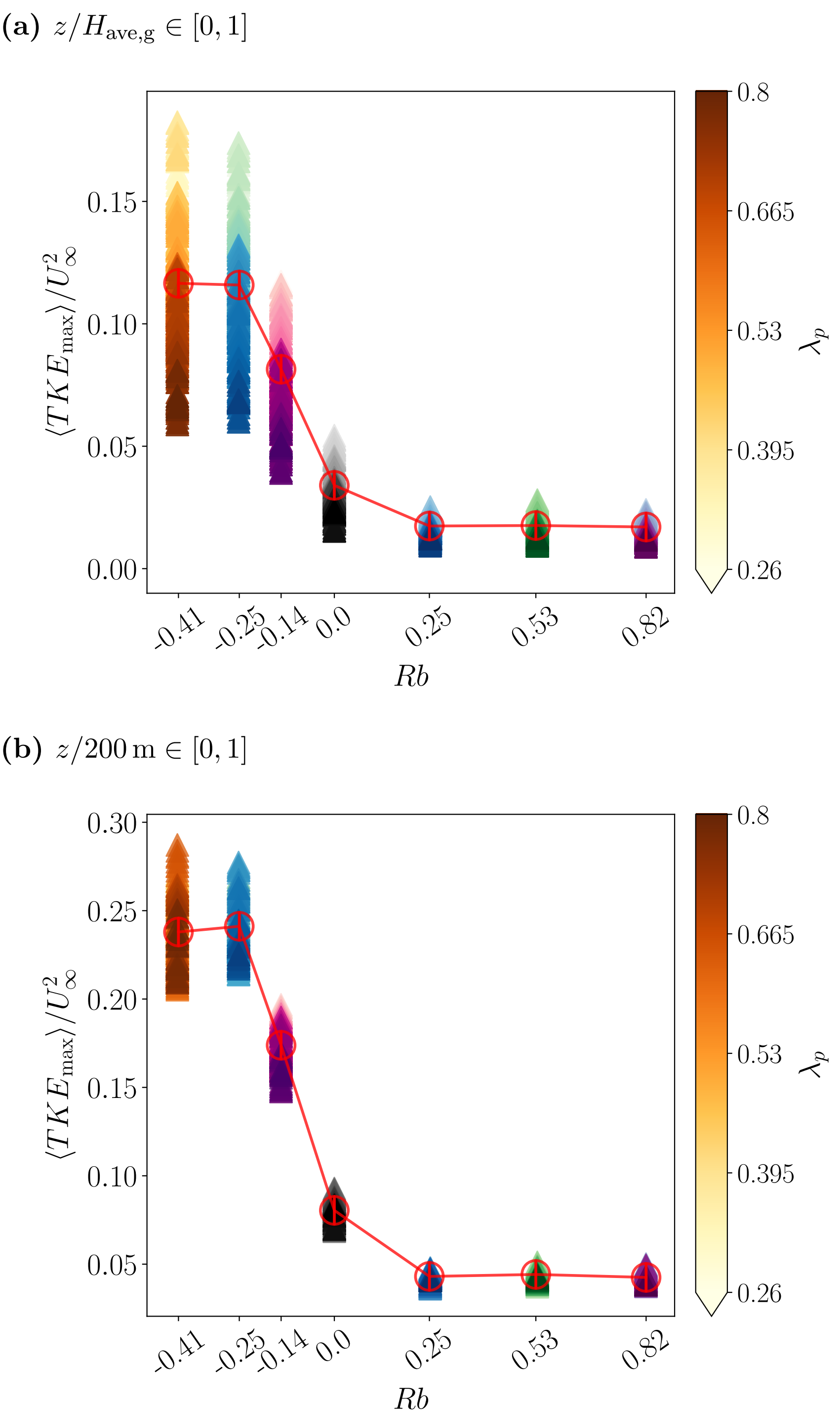

Figure 14: Spatial and ensemble averages of the normalised gustiness TKE, TKE_{max}, versus Rb for (a) $z/H_{\text{ave,g}} \in [0, 1]$ and (b) $z/200\,\text{m} \in [0, 1]$. The colormaps sketch the change of λ_p. Following the same convention, deep colors correspond to large λ_p and light to small λ_p. For brevity, the colorbar is only shown for the most unstable case ($\text{Rb} = -0.41$). The solid line connects the ensemble averages (denoted using the angle brackets, Eq. (9)) of TKE_{max} associated with each Rb.

(a) $z/H_{\mathrm{ave,g}} \in [0, 1]$

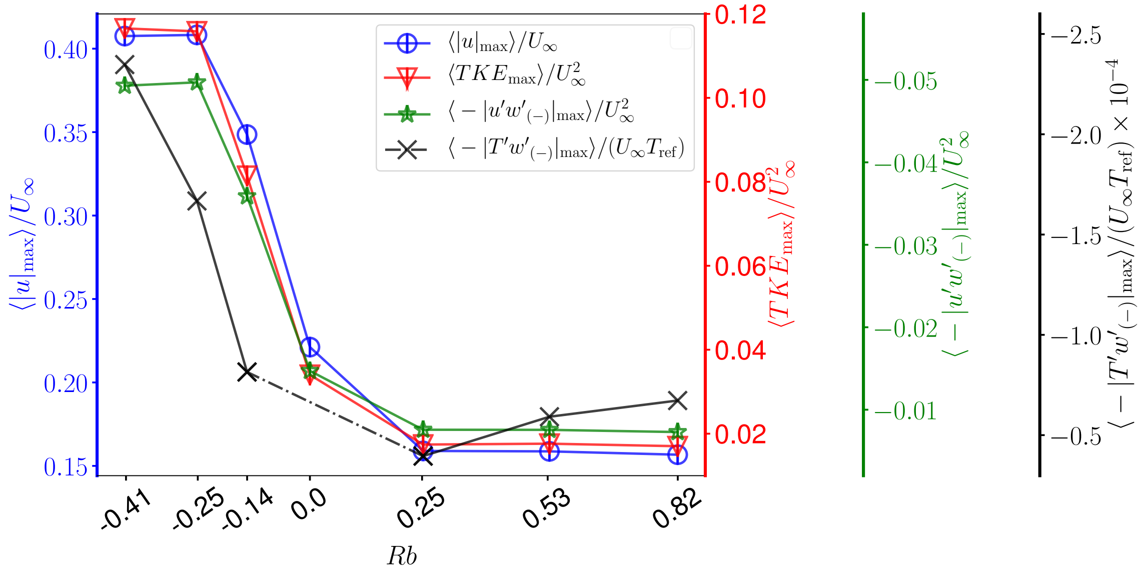

(b) $z/200\,\mathrm{m} \in [0, 1]$

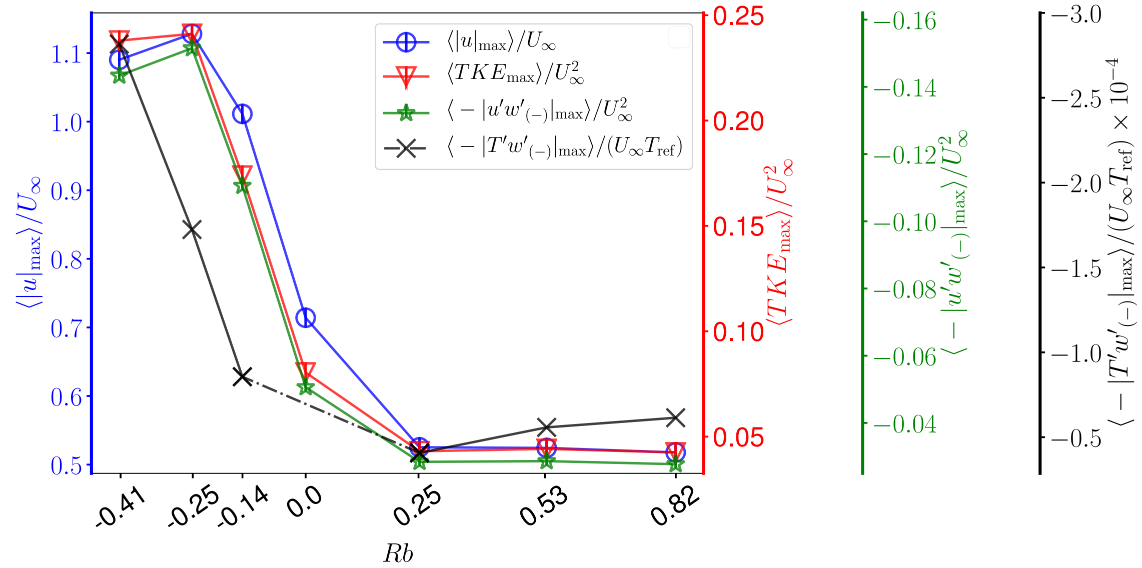

Figure 15: As in Fig. 14, but a summary of the sensitivity of the zeroth- and second-order gustiness statistics, Eq. (16), to the boundary-layer stability. **The angle brackets denote the ensemble average over all sampling units, Eq. (9). Note the y-axis values that are plotted in reverse order for the gustiness fluxes.**

6. Summary and discussion

This research investigated **gustiness** in thermally-stratified turbulent boundary-layer flows for a real urban topography using LES. **It complements previous studies (e.g. Ahmad et al., 2017; Takemi et al., 2020), wherein the focus was primarily on wind gusts outreaching the time-averaged wind speed in neutrally-stratified urban boundary layers, in the aspects that gustiness were explored for** the zeroth-order (the local maximum wind speed), first-order (the local maximum wind fluctuation) and second-order (local maxima of turbulence intensities and fluxes) statistics for a wide range of boundary-layer stabilities, $\mathrm{Rb} \in [-0.41,\ 0.82]$, that satisfy observations of realistic urban TBLs. **The results were obtained based on a proposed ensemble sampling approach across the domain, which allows the analysis to be performed in statistical manner and hence a more comprehensive characterisation of the urban surface heterogeneity.**

The contribution of this study includes the following findings. 1. The strong linear scaling of the gustiness statistics ($\mathcal{G}$) with the plan-area index (λ_p) for neutral flow is found to persist for stable and unstable stratification. 2. There is a similar trend for $\mathcal{G}$ versus the other topographic parameters ($\mathcal{S}$): the frontal-area index (λ_f) and the building-height variability (σ_H); however, their scaled forms, $\lambda_f H_{\mathrm{ave}}/\sigma_H$ and $\sigma_H/H_{\mathrm{ave}}$, are argued to be of more appropriateness as scaling parameters for $\mathcal{G}$. 3. While the monotonic dependence of $\mathcal{G}$ on $\mathcal{S}$ appears to be well maintained across $z/H_{\mathrm{ave}} \lesssim 1$, the influence of $\mathcal{S}$ on $\mathcal{G}$ is less definite at greater heights. 4. The gustiness increases monotonically with the boundary-layer instability and plateaus for stable flow, in accord with the sensitivity for the conventional mean and turbulence statistics. 5. Qualitative differences in the sensitivities to the boundary-layer stability are narrowly distinguishable amongst the proposed gustiness statistics.

The results are obtained for a realistic urban topography. It is plausible that the conclusions would carry over to urban cities of comparable morphological metrics, e.g. Kyoto, London or Berlin. **For example, Kyoto city centre is characterised with a mean building height of $10.8\,\mathrm{m} \pm 7.0\,\mathrm{m}$ (Yoshida et al., 2018), which is almost the same as that investigated in the current study ($11.5\,\mathrm{m} \pm 7.1\,\mathrm{m}$, see Sec. 2.1). While the building packing indices ($\lambda_f = 0.25$ and $\lambda_p = 0.41$) are slightly smaller, the values lie well within the range covered by the urban** areas herein (Sec. 2.2). However, further work may be required to verify the robustness of the results for cities like Los Angeles. Although the building packing densities are comparable to Osaka, the mean building height ($51.3\,\mathrm{m}$) of Los Angeles (Ratti et al., 2002) is almost five times larger and the non-dimensional building height variability ($\sigma_{H,\mathrm{g}}/H_{\mathrm{ave,g}}$) is also much greater than that considered in the current study (1.0 versus 0.6).

One limitation of this study is only unidirectional wind was considered. It is unlikely that the conclusions for λ_p and σ_H versus $\mathcal{G}$ would be affected; however, the frontal-area index, λ_f, differs when the wind direction is changed. More efforts would be demanded to verify the scaling of $\mathcal{G}$ with the proposed effective λ_f, $\hat{\lambda}_f$. Another limitation is that the flow is driven by a steady forcing through a prescribed pressure gradient and thermal stratification generated by fixed temperature differences (Duan and Ngan, 2019). For urban wind hazards, it may be of more relevance if unsteady perturbations from mesoscale model output or observations, in particular of strong tropical cyclones (Islam et al., 2015; Takemi and Ito, 2020), could be incorporated into building-resolving LES. While the proposed sampling approach allows ensemble averaging and analyses in a statistical manner, the conclusions for $\mathcal{G}$ versus $\mathcal{S}$ may not be anticipated for a very local urban district and influences of architecture contours, e.g. building roof shapes and the 3-D details of specific building obstacles (Korycki et al., 2016), may be of potential interest for future investigation.

Acknowledgements

This study was supported by the Environment Research and Technology Development Fund JPMEERF20192005 of the Environmental Restoration and Conservation Agency of Japan and Japan Society for Promotion of Sciences Kakenhi 18H01680. The computation used the Large-Scale Computer Systems, Laurel 2, Kyoto University. The authors thank the anonymous referes for helpful comments and suggestions.

References

Bhagirath Addepalli and Eric R. Pardyjak. Investigation of the flow structure in step-up street canyons-mean flow and turbulence statistics. *Boundary-Layer Meteorology*, 148 (1):133–155, 2013. ISSN 1573-1472. doi: 10.1007/s10546-013-9810-5.

Nurul Huda Ahmad, Atsushi Inagaki, Manabu Kanda, Naoyuki Onodera, and Takayuki Aoki. Large-eddy simulation of the gust index in an urban area using the lattice boltzmann method. *Boundary-Layer Meteorology*, 163(3):447–467, Jun 2017. ISSN 1573-1472. doi: 10.1007/s10546-017-0233-6.

Jonas Allegrini. A wind tunnel study on three-dimensional buoyant flows in street canyons with different roof shapes and building lengths. *Building and Environment*, 143:71 – 88, 2018. ISSN 0360-1323. doi: https://doi.org/10.1016/j.buildenv.2018.06.056.

William Anderson, Qi Li, and Elie Bou-Zeid. Numerical simulation of flow over urban-like topographies and evaluation of turbulence temporal attributes. *Journal of Turbulence*, 16(9):809–831, 2015. doi: 10.1080/14685248.2015.1031241.

Yasunobu Ashie and Takaaki Kono. Urban-scale cfd analysis in support of a climate-sensitive design for the tokyo bay area. *International Journal of Climatology*, 31(2): 174–188, 2011. ISSN 1097-0088. doi: 10.1002/joc.2226.

Stephen E Belcher. Mixing and transport in urban areas. *Philosophical Transactions of the Royal Society A: Mathematical, Physical and Engineering Sciences*, 363(1837): 2947–2968, 2005. doi: 10.1098/rsta.2005.1673.

Elie Bou-Zeid, Jan Overney, Benedict D. Rogers, and Marc B. Parlange. The effects of building representation and clustering in large-eddy simulations of flows in urban canopies. *Boundary-Layer Meteorology*, 132(3):415–436, Sep 2009. ISSN 1573-1472. doi: 10.1007/s10546-009-9410-6.

Elie Bou-Zeid, Chad Higgins, Hendrik Huwald, Charles Meneveau, and Marc B. Parlange. Field study of the dynamics and modelling of subgrid-scale turbulence in a stable atmospheric surface layer over a glacier. *Journal of Fluid Mechanics*, 665:480515, 2010. doi: 10.1017/S0022112010004015.

R. E. Britter and S. R. Hanna. Flow and dispersion in urban areas. *Annual Review of Fluid Mechanics*, 35(1):469–496, 2003.

H. Cheng, P. Hayden, A.G. Robins, and I.P. Castro. Flow over cube arrays of different packing densities. *Journal of Wind Engineering and Industrial Aerodynamics*, 95(8): 715 – 740, 2007. ISSN 0167-6105. doi: http://dx.doi.org/10.1016/j.jweia.2007.01.004.

Hong Cheng and Ian P. Castro. Near wall flow over urban-like roughness. *Boundary-Layer Meteorology*, 104(2):229–259, 2002. ISSN 0006-8314. doi: 10.1023/A:1016060103448.

W.C. Cheng and Chun-Ho Liu. Large-eddy simulation of turbulent transports in urban street canyons in different thermal stabilities. *Journal of Wind Engineering and Industrial Aerodynamics*, 99(4):434 – 442, 2011. ISSN 0167-6105. doi: http://dx.doi.org/10.1016/j.jweia.2010.12.009. The Fifth International Symposium on Computational Wind Engineering.

O. Coceal, A. Dobre, T. G. Thomas, and S. E. Belcher. Structure of turbulent flow over regular arrays of cubical roughness. *Journal of Fluid Mechanics*, 589:375409, 2007a. doi: 10.1017/S002211200700794X.

Omduth Coceal, T. Glyn Thomas, and Stephen E. Belcher. Spatial variability of flow statistics within regular building arrays. *Boundary-Layer Meteorology*, 125(3):537–552, Dec 2007b. ISSN 1573-1472. doi: 10.1007/s10546-007-9206-5.

Zhiqiang Cui, Xiaoming Cai, and Chris J. Baker. Large-eddy simulation of turbulent flow in a street canyon. *Quarterly Journal of the Royal Meteorological Society*, 130(599): 1373–1394, 2004. ISSN 1477-870X. doi: 10.1256/qj.02.150.

James W. Deardorff. Stratocumulus-capped mixed layers derived from a three-dimensional model. *Boundary-Layer Meteorology*, 18(4):495–527, 1980.

H. W. Detering and D. Etling. Application of the E-ϵ turbulence model to the atmospheric boundary layer. *Boundary-Layer Meteorology*, 33(2):113–133, Oct 1985. ISSN 1573-1472. doi: 10.1007/BF00123386.

G. Duan and K. Ngan. Effects of time-dependent inflow perturbations on turbulent flow in a street canyon. *Boundary-Layer Meteorology*, 167(2):257–284, May 2018. ISSN 1573-1472. doi: 10.1007/s10546-017-0327-1.

G. Duan and K. Ngan. Sensitivity of turbulent flow around a 3-D building array to urban boundary-layer stability. *Journal of Wind Engineering and Industrial Aerodynamics*, 193:103958, 2019. ISSN 0167-6105. doi: https://doi.org/10.1016/j.jweia.2019.103958.

G. Duan and K. Ngan. Influence of thermal stability on the ventilation of a 3-d building array. *Building and Environment*, 106969, 2020. doi: https://doi.org/10.1016/j.buildenv.2020.106969.

Y. Dubief and F. Delcayre. On coherent-vortex identification in turbulence. *Journal of Turbulence*, 1:011, December 2000. doi: 10.1088/1468-5248/1/1/011.

Jiannong Fang and Fernando Porté-Agel. Large-eddy simulation of very-large-scale motions in the neutrally stratified atmospheric boundary layer. *Boundary-Layer Meteorology*, 155(3):397–416, Jun 2015. ISSN 1573-1472. doi: 10.1007/s10546-015-0006-z.

M. G. Giometto, A. Christen, C. Meneveau, J. Fang, M. Krafczyk, and M. B. Parlange. Spatial characteristics of roughness sublayer mean flow and turbulence over a realistic urban surface. *Boundary-Layer Meteorology*, 160(3):425–452, 2016. ISSN 1573-1472. doi: 10.1007/s10546-016-0157-6.

C. S. B. Grimmond and T. R. Oke. Aerodynamic properties of urban areas derived from analysis of surface form. *Journal of Applied Meteorology*, 38(9):1262–1292, 1999. doi: 10.1175/1520-0450(1999)038⟨1262:APOUAD⟩2.0.CO;2.

Tobias Gronemeier, Siegfried Raasch, and Edward Ng. Effects of unstable stratification on ventilation in Hong Kong. *Atmosphere*, 8(9):168, 2017.

Aya Hagishima, Jun Tanimoto, Koji Nagayama, and Sho Meno. Aerodynamic parameters of regular arrays of rectangular blocks with various geometries. *Boundary-Layer Meteorology*, 132(2):315–337, 2009. ISSN 1573-1472. doi: 10.1007/s10546-009-9403-5.

Steven R. Hanna, Michael J. Brown, Fernando E. Camelli, Stevens T. Chan, William J. Coirier, Sura Kim, Olav R. Hansen, Alan H. Huber, and R. Michael Reynolds. Detailed simulations of atmospheric flow and dispersion in downtown Manhattan: An application of five computational fluid dynamics models. *Bulletin of the American Meteorological Society*, 87(12):1713–1726, 2006. doi: 10.1175/BAMS-87-12-1713.

Taiichi Hayashi. Gust and downward momentum transport in the atmospheric surface layer. *Boundary-Layer Meteorology*, 58(1):33–49, 1992. ISSN 1573-1472.

Jianming He and Charles C.S Song. Evaluation of pedestrian winds in urban area by numerical approach. *Journal of Wind Engineering and Industrial Aerodynamics*, 81(1): 295 – 309, 1999. ISSN 0167-6105. doi: https://doi.org/10.1016/S0167-6105(99)00025-2.

Walter G. Hoydysh and Walter F. Dabberdt. Kinematics and dispersion characteristics of flows in asymmetric street canyons. *Atmospheric Environment (1967)*, 22(12):2677 – 2689, 1988. ISSN 0004-6981. doi: https://doi.org/10.1016/0004-6981(88)90436-2.

L.J. Hunter, G.T. Johnson, and I.D. Watson. An investigation of three-dimensional characteristics of flow regimes within the urban canyon. *Atmospheric Environment. Part B. Urban Atmosphere*, 26(4):425 – 432, 1992. ISSN 0957-1272. doi: http://dx.doi.org/10.1016/0957-1272(92)90049-X.

M. Hussain and B.E. Lee. A wind tunnel study of the mean pressure forces acting on large groups of low-rise buildings. *Journal of Wind Engineering and Industrial Aerodynamics*, 6(3):207 – 225, 1980. ISSN 0167-6105. doi: http://dx.doi.org/10.1016/0167-6105(80)90002-1.

N. Hutchins and Ivan Marusic. Evidence of very long meandering features in the logarithmic region of turbulent boundary layers. *Journal of Fluid Mechanics*, 579:128, 2007. doi: 10.1017/S0022112006003946.

A. Inagaki and M. Kanda. Turbulent flow similarity over an array of cubes in near-neutrally stratified atmospheric flow. *Journal of Fluid Mechanics*, 615:101–120, 11 2008. ISSN 1469-7645. doi: 10.1017/S0022112008003765.

Tanvir Islam, Prashant K. Srivastava, Miguel A. Rico-Ramirez, Qiang Dai, Manika Gupta, and Sudhir K. Singh. Tracking a tropical cyclone through wrf–arw simulation and sensitivity of model physics. *Natural Hazards*, 76(3):1473–1495, Apr 2015. ISSN 1573-0840. doi: 10.1007/s11069-014-1494-8.

Isao Kanda and Yukio Yamao. Passive scalar diffusion in and above urban-like roughness under weakly stable and unstable thermal stratification conditions. *Journal of Wind Engineering and Industrial Aerodynamics*, 148:18–33, 2016. ISSN 0167-6105.

Manabu Kanda, Atsushi Inagaki, Takashi Miyamoto, Micha Gryschka, and Siegfried Raasch. A new aerodynamic parametrization for real urban surfaces. *Boundary-Layer Meteorology*, 148(2):357–377, Aug 2013. ISSN 1573-1472. doi: 10.1007/s10546-013-9818-x.

Petra Kastner-Klein and Mathias W. Rotach. Mean flow and turbulence characteristics in an urban roughness sublayer. *Boundary-Layer Meteorology*, 111(1):55–84, 2004. ISSN 1573-1472. doi: 10.1023/B:BOUN.0000010994.32240.b1.

Marius Keck, Siegfried Raasch, Marcus Letzel, and Edward Ng. First results of high resolution large-eddy simulations of the atmospheric boundary layer in macau. *Journal of Heat Island Institute International*, 9:39–43, 12 2014.

H. Knoop, F. Ament, and B. Maronga. A generic gust definition and detection method based on wavelet-analysis. *Advances in Science and Research*, 16:143–148, 2019. doi: 10.5194/asr-16-143-2019.

Michał Korycki, Lech Łobocki, and Andrzej Wyszogrodzki. Numerical simulation of stratified flow around a tall building of a complex shape. *Environmental Fluid Mechanics*, 16(6):1143–1171, Dec 2016. ISSN 1573-1510.

Marcus Oliver Letzel, Martina Krane, and Siegfried Raasch. High resolution urban large-eddy simulation studies from street canyon to neighbourhood scale. *Atmospheric Environment*, 42(38):8770–8784, 2008.

Dan Li and Elie Bou-Zeid. Coherent structures and the dissimilarity of turbulent transport of momentum and scalars in the unstable atmospheric surface layer. *Boundary-Layer Meteorology*, 140(2):243–262, Aug 2011. ISSN 1573-1472. doi: 10.1007/s10546-011-9613-5.

K. W. Lo and K. Ngan. Characterizing ventilation and exposure in street canyons using Lagrangian particles. *Journal of Applied Meteorology and Climatology*, 56(5):1177–1194, 2017. doi: 10.1175/JAMC-D-16-0168.1.

S. Rajagopalan M. R. Raupach, R. A. Antonia. Rough-wall turbulent boundary layers. *Applied Mechanics Reviews*, 4(1):1–25, 1991. doi: https://doi.org/10.1115/1.3119492.

R.W. Macdonald, R.F. Griffiths, and D.J. Hall. An improved method for the estimation of surface roughness of obstacle arrays. *Atmospheric Environment*, 32(11):1857 – 1864, 1998. ISSN 1352-2310. doi: http://dx.doi.org/10.1016/S1352-2310(97)00403-2.

B. Maronga, M. Gryschka, R. Heinze, F. Hoffmann, F. Kanani-Sühring, M. Keck, K. Ketelsen, M. O. Letzel, M. Sühring, and S. Raasch. The parallelized large-eddy simulation model (PALM) version 4.0 for atmospheric and oceanic flows: model formulation, recent developments, and future perspectives. *Geoscientific Model Development*, 8(8): 2515–2551, 2015. doi: 10.5194/gmd-8-2515-2015.

Davide Marucci and Matteo Carpentieri. Effect of local and upwind stratification on flow and dispersion inside and above a bi-dimensional street canyon. *Building and Environment*, 156:74 – 88, 2019. ISSN 0360-1323. doi: https://doi.org/10.1016/j.buildenv.2019.04.013.

Davide Marucci and Matteo Carpentieri. Stable and convective boundary-layer flows in an urban array. *Journal of Wind Engineering and Industrial Aerodynamics*, 200: 104140, 2020. ISSN 0167-6105. doi: https://doi.org/10.1016/j.jweia.2020.104140.

Takenobu Michioka, Hiroshi Takimoto, Hiroki Ono, and Ayumu Sato. Large-eddy simulation of the effects of wind-direction fluctuations on turbulent flow and gas dispersion within a cubical canopy. *Boundary-Layer Meteorology*, Jul 2019. ISSN 1573-1472. doi: 10.1007/s10546-019-00467-y.

Chin-Hoh Moeng and John C. Wyngaard. Spectral analysis of large-eddy simulations of the convective boundary layer. *Journal of the Atmospheric Sciences*, 45(23):3573–3587, 1988.

Wim Munters, Charles Meneveau, and Johan Meyers. Shifted periodic boundary conditions for simulations of wall-bounded turbulent flows. *Physics of Fluids*, 28(2):025112, 2016. doi: 10.1063/1.4941912.

Shuzo Murakami and Kunio Fujii. Turbulence characteristics of wind flow at ground level in built-up area. *Journal of Wind Engineering & Industrial Aerodynamics*, 15 (1-3):133–144, 1983.

F. Murena, A. Di Benedetto, M. D'Onofrio, and G. Vitiello. Mass transfer velocity and momentum vertical exchange in simulated deep street canyons. *Boundary-Layer Meteorology*, 140(1):125–142, 2011.

Fabio Murena and Benedetto Mele. Effect of short-time variations of wind velocity on mass transfer rate between street canyons and the atmospheric boundary layer. *Atmospheric Pollution Research*, 2014, Vol. 5:p484, 2014.

Y. Nakamura and T.R. Oke. Wind, temperature and stability conditions in an east-west oriented urban canyon. *Atmospheric Environment (1967)*, 22(12):2691 – 2700, 1988. ISSN 0004-6981. doi: http://dx.doi.org/10.1016/0004-6981(88)90437-4.

Hiromasa Nakayama, Tetsuya Takemi, and Haruyasu Nagai. LES analysis of the aerodynamic surface properties for turbulent flows over building arrays with various geometries. *Journal of Applied Meteorology and Climatology*, 50(8):1692–1712, 2011. doi: 10.1175/2011JAMC2567.1.

Hiromasa Nakayama, Tetsuya Takemi, and Haruyasu Nagai. Large-eddy simulation of urban boundary-layer flows by generating turbulent inflows from mesoscale meteorological simulations. *Atmospheric Science Letters*, 13(3):180–186, 2012. doi: 10.1002/asl.377.

N. Nazarian and J. Kleissl. Realistic solar heating in urban areas: Air exchange and street-canyon ventilation. *Building and Environment*, 95:75 – 93, 2016. ISSN 0360-1323. doi: http://dx.doi.org/10.1016/j.buildenv.2015.08.021.

K. Ngan and K. W. Lo. Revisiting the flow regimes for urban street canyons using the numerical green's function. *Environmental Fluid Mechanics*, 16(2):313–334, Apr 2016. ISSN 1573-1510. doi: 10.1007/s10652-015-9422-3.

K. Ngan and K. W. Lo. Linear error dynamics for turbulent flow in urban street canyons. *Journal of Applied Meteorology and Climatology*, 56(5):1195–1208, 2017. doi: 10.1175/JAMC-D-16-0173.1.

Tim R Oke. Initial guidance to obtain representative meteorological observations at urban sites. *INSTRUMENTS AND OBSERVING METHODS REPORT No. 81, WMO/TD-No. 1250*, 2006.

Seung-Bu Park and Jong-Jin Baik. A large-eddy simulation study of thermal effects on turbulence coherent structures in and above a building array. *Journal of Applied Meteorology and Climatology*, 52(6):1348–1365, 2013.

Seung-Bu Park, Jong-Jin Baik, and Beom-Soon Han. Large-eddy simulation of turbulent flow in a densely built-up urban area. *Environmental Fluid Mechanics*, 15(2):235–250, Apr 2015. ISSN 1573-1510. doi: 10.1007/s10652-013-9306-3.

A. E. Perry, W. H. Schofield, and P. N. Joubert. Rough wall turbulent boundary layers. *Journal of Fluid Mechanics*, 37(2):383413, 1969. doi: 10.1017/S0022112069000619.

C. Ratti, S. Di Sabatino, R. Britter, M. Brown, F. Caton, and S. Burian. Analysis of 3-d urban databases with respect to pollution dispersion for a number of european and american cities. *Water, Air and Soil Pollution: Focus*, 2(5):459–469, 2002. ISSN 1573-2940.

M. R. Raupach. Drag and drag partition on rough surfaces. *Boundary-Layer Meteorology*, 60(4):375–395, 1992. ISSN 1573-1472.

M. R. Raupach, J. J. Finnigan, and Y. Brunei. Coherent eddies and turbulence in vegetation canopies: The mixing-layer analogy. *Boundary-Layer Meteorology*, 78(3): 351–382, 1996. ISSN 1573-1472. doi: 10.1007/BF00120941.

M. W. Rotach. Profiles of turbulence statistics in and above an urban street canyon. *Atmospheric Environment*, 29(13):1473–1486, 1995.

Matthias Roth, Atsushi Inagaki, Hirofumi Sugawara, and Manabu Kanda. Small-scale spatial variability of turbulence statistics, (co)spectra and turbulent kinetic energy measured over a regular array of cube roughness. *Environmental Fluid Mechanics*, 15 (2):329–348, Apr 2015. ISSN 1573-1510. doi: 10.1007/s10652-013-9322-3.

Roger H Shaw and A.R Pereira. Aerodynamic roughness of a plant canopy: A numerical experiment. *Agricultural Meteorology*, 26(1):51 – 65, 1982. ISSN 0002-1571. doi: https://doi.org/10.1016/0002-1571(82)90057-7.

Mark W. Simpson and Ari Glezer. Buoyancy-induced, columnar vortices. *Journal of Fluid Mechanics*, 804:712748, 2016. doi: 10.1017/jfm.2016.541.

Tetsuya Takemi and Rui Ito. Benefits of high-resolution downscaling experiments for assessing strong wind hazard at local scales in complex terrain: a case study of typhoon songda (2004). *Progress in Earth and Planetary Science*, 7(1):4, 2020. ISSN 2197-4284.

Tetsuya Takemi, Toshiya Yoshida, Shota Yamasaki, and Kentaro Hase. Quantitative estimation of strong winds in an urban district during typhoon jebi (2018) by merging mesoscale meteorological and large-eddy simulations. *SOLA*, 15:22–27, 2019. doi: 10.2151/sola.2019-005.

Tetsuya Takemi, Toshiya Yoshida, Mitsuaki Horiguchi, and Wim Vanderbauwhede. Large-eddy-simulation analysis of airflows and strong wind hazards in urban areas. *Urban Climate*, 32:100625, 2020. ISSN 2212-0955. doi: https://doi.org/10.1016/j.uclim.2020.100625.

Christoph Thomas and Thomas Foken. Organised motion in a tall spruce canopy: Temporal scales, structure spacing and terrain effects. *Boundary-Layer Meteorology*, 122 (1):123–147, Jan 2007. ISSN 1573-1472. doi: 10.1007/s10546-006-9087-z.

Kiyoshi Uehara, Shuzo Murakami, Susumu Oikawa, and Shinji Wakamatsu. Wind tunnel experiments on how thermal stratification affects flow in and above urban street canyons. *Atmospheric Environment*, 34(10):1553 – 1562, 2000. ISSN 1352-2310. doi: http://dx.doi.org/10.1016/S1352-2310(99)00410-0.

James M. Wallace. Quadrant analysis in turbulence research: History and evolution. *Annual Review of Fluid Mechanics*, 48(1):131–158, 2016. doi: 10.1146/annurev-fluid-122414-034550.

C. Wang and W. Anderson. Turbulence coherence within canonical and realistic aeolian dune-field roughness sublayers. *Boundary-Layer Meteorology*, 173(3):409–434, Dec 2019. ISSN 1573-1472. doi: 10.1007/s10546-019-00477-w.

Huanhuan Wang, Peter Brimblecombe, and Keith Ngan. Particulate matter inside and around elevated walkways. *Science of The Total Environment*, page 134256, 2019. ISSN 0048-9697. doi: https://doi.org/10.1016/j.scitotenv.2019.134256.

Weiwen Wang and Edward Ng. Air ventilation assessment under unstable atmospheric stratification-a comparative study for hong kong. *Building and Environment*, 130:1 – 13, 2018a. ISSN 0360-1323. doi: https://doi.org/10.1016/j.buildenv.2017.12.018.

Weiwen Wang and Edward Ng. Large-eddy simulations of air ventilation in parametric scenarios: comparative studies of urban form and wind direction. *Architectural Science Review*, 0(0):1–11, 2018b. doi: 10.1080/00038628.2018.1481359.

Louis J. Wicker and William C. Skamarock. Time-splitting methods for elastic models using forward time schemes. *Monthly weather review*, 130(8):2088–2097, August 2002. ISSN 0027-0644. doi: 10.1175/1520-0493(2002)130⟨2088:TSMFEM⟩2.0.CO;2.

J. H. Williamson. Low-storage runge-kutta schemes. *Journal of Computational Physics*, 35(1):48–56, 1980.

R. A. Wooding, E. F. Bradley, and J. K. Marshall. Drag due to regular arrays of roughness elements of varying geometry. *Boundary-Layer Meteorology*, 5(3):285–308, Jul 1973. ISSN 1573-1472. doi: 10.1007/BF00155238.

Jie-Zhi Wu, Hui-Yang Ma, and Ming-De Zhou. *Vorticity and Vortex Dynamics*. Springer-Verlag Berlin Heidelberg, 2006. doi: 10.1007/978-3-540-29028-5.

Zheng-Tong Xie, Omduth Coceal, and Ian P. Castro. Large-eddy simulation of flows over random urban-like obstacles. *Boundary-Layer Meteorology*, 129(1):1, Aug 2008. ISSN 1573-1472. doi: 10.1007/s10546-008-9290-1.

Neda Yaghoobian, Jan Kleissl, and Kyaw Tha Paw U. An improved three-dimensional simulation of the diurnally varying street-canyon flow. *Boundary-Layer Meteorology*, 153(2):251–276, 2014. ISSN 0006-8314. doi: 10.1007/s10546-014-9940-4.

Mohamed F Yassin and Masaake Ohba. Experimental simulation of air quality in street canyon under changes of building orientation and aspect ratio. *J Expos Sci Environ Epidemiol*, 22(5):502–515, September 2012. ISSN 1559-0631.

Toshiya Yoshida and Tetsuya Takemi. Properties of mixing length and dispersive stress in airflows over urban-like roughness obstacles with variable height. *SOLA*, 14:174–178, 2018. doi: 10.2151/sola.2018-031.

Toshiya Yoshida, Tetsuya Takemi, and Mitsuaki Horiguchi. Large-eddy-simulation study of the effects of building-height variability on turbulent flows over an actual urban area. *Boundary-Layer Meteorology*, 168(1):127–153, 2018. ISSN 1573-1472.